Electron microscopy observations of the diversity of Ryugu organic matter and its relationship to minerals at the micro-to nano-scale

Rhonda M Stroud, Jens Barosch, Lydie Bonal, Katherine Burgess, George D Cody, Bradley T de Gregorio, Luke Daly, Emmanuel Dartois, Jean Duprat, Cecile Engrand, et al.

The Meteoritical Society

Meteoritics & Planetary Science 1–21 (2024)
doi: 10.1111/maps.14128

Electron microscopy observations of the diversity of Ryugu organic matter and its relationship to minerals at the micro- to nano-scale

Rhonda M. STROUD[1,2]*, Jens BAROSCH[3], Lydie BONAL[4], Katherine BURGESS[2], George D. CODY[3], Bradley T. DE GREGORIO[2], Luke DALY[5,6,7], Emmanuel DARTOIS[8], Elena DOBRICĂ[9], Jean DUPRAT[10], Cecile ENGRAND[11], Dennis HARRIES[12], Minako HASHIGUCHI[13], Hope ISHII[9], Yoko KEBUKAWA[14], A. David KILCOYNE, Falko LANGENHORST[15], Martin R. LEE[5], Larry R. NITTLER[1,3], Eric QUIRICO[4], Taiga OKUMURA[16], Laurent REMUSAT[10], Scott SANDFORD[17], Hikaru YABUTA[18], Masanao ABE[19,20], Neyda M. ABREU[21], Paul A. J. BAGOT[7], Pierre BECK[4], Laure BEJACH[11], Phil A. BLAND[22], John C. BRIDGES[23], Brittany A. CYMES[2], Alexandre DAZZI[24], Francisco de la PEÑA[25], Ariane DENISET-BESSEAU[24], Satomi ENJU[26], Yuma ENOKIDO[27], David R. FRANK[9], Jennifer GRAY[28], Mitsutaka HARUTA[29], Satoshi HATA[30,31], Leon HICKS[32], Yohei IGAMI[33], Damien JACOB[25], Kanami KAMIDE[18], Mutsumi KOMATSU[34], Sylvain LAFORET[25], Hugues LEROUX[25], Corentin LE GUILLOU[25], Zita MARTINS[35], Maya MARINOVA[25], James MARTINEZ[36], Jérémie MATHURIN[24], Megumi MATSUMOTO[27], Toru MATSUMOTO[33,37], Junya MATSUNO[38], Samuel MCFADZEAN[39], Tatsuhiro MICHIKAMI[40], Itaru MITSUKAWA[31], Akira MIYAKE[33], Masaaki MIYAHARA[18], Akiko MIYAZAKI[41], Gilles MONTAGNAC[42], Smail MOSTEFAOUI[10], Tomoki NAKAMURA[27], Aiko NAKATO[19], Hiroshi NARAOKA[43], Yusuke NAKAUCHI[19], Satoru NAKAZAWA[19], Masahiro NISHIMURA[19], Takaaki NOGUCHI[34], Kenta OHTAKI[9], Takuji OHIGASHI[44], Tatsuaki OKADA[19,20], Shota OKUMURA[33], Ryuji OKAZAKI[45], Thi H. V. PHAN[4], Rolando REBOIS[4], Kanako SAKAMOTO[19], Takanao SAIKI[19], Hikaru SAITO[30,31], Yusuke SETO[18], Miho SHIGENAKA[18], William SMITH[39], Hiroki SUGA[46], Mingqi SUN[46], Shogo TACHIBANA[16,19], Yoshio TAKAHASHI[16], Yasuo TAKEICHI[47], Akihisa TAKEUCHI[46], Aki TAKIGAWA[16], Yusuke TAMENORI[46], Satoshi TANAKA[19], Fuyuto TERUI[48], Michelle S. THOMPSON[49], Naotaka TOMIOKA[50], Akira TSUCHIYAMA[51], Yuichi TSUDA[19], Kentaro UESUGI[46], Masayuki UESUGI[46], Tomohiro USUI[19], Maximilien VERDIER-PAOLETTI[10], Daisuke WAKABAYASHI[47], Sei-ichiro WATANABE[52], Toru YADA[19], Shohei YAMASHITA[47], Masahiro YASUTAKE[46], Kasumi YOGATA[19], Makoto YOSHIKAWA[19], Hisayoshi YURIMOTO[53], Pierre-M. ZANETTA[54], Thomas ZEGA[54], and Michael E. ZOLENSKY[55]

[1]School of Earth and Space Exploration, Arizona State University, Tempe, Arizona, USA
[2]Materials Science and Technology Division, US Naval Research Laboratory, Washington, DC, USA
[3]Earth and Planets Laboratory, Carnegie Institution for Science, Washington, DC, USA
[4]Institut de Planétologie et d'Astrophysique, Université Grenoble Alpes, Grenoble, France
[5]School of Geographical and Earth Sciences, University of Glasgow, Glasgow, UK
[6]Australian Centre for Microscopy and Microanalysis, University of Sydney, Sydney, New South Wales, Australia
[7]Department of Materials, University of Oxford, Oxford, UK
[8]Institut des Sciences Moléculaires d'Orsay, Université Paris-Saclay, Centre National de la Recherche Scientifique, Orsay, France
[9]Hawai'i Institute of Geophysics and Planetology, the University of Hawai'i at Mānoa, Honolulu, Hawaii, USA
[10]Institut de Mineralogie, Physique des Materiaux et Cosmochimie, Museum National d'Histoire Naturelle, Centre National de la Recherche Scientifique UMR 7590, Sorbonne Université, Paris, France
[11]Laboratoire de Physique des 2 Infinis Irène Joliot-Curie, Centre National de la Recherche Scientifique, Université Paris-Saclay, Orsay, France
[12]Luxembourg Institute of Science and Technology, European Space Resources Innovation Centre, Belvaux, Luxembourg

[13]Graduate School of Environmental Studies, Nagoya University, Nagoya, Japan
[14]Department of Chemistry and Life Science, Yokohama National University, Yokohama, Japan
[15]Institute of Geoscience, Friedrich Schiller University Jena, Jena, Germany
[16]Department of Earth and Planetary Science, The University of Tokyo, Tokyo, Japan
[17]NASA Ames Research Center, Moffett Field, California, USA
[18]Department of Earth and Planetary Systems Science, Hiroshima University, Hiroshima, Japan
[19]Institute of Space and Astronautical Science, Japan Aerospace Exploration Agency, Sagamihara, Kanagawa, Japan
[20]The Graduate University for Advanced Studies, SOKENDAI, Hayama, Japan
[21]Langley Research Center, NASA, Hampton, Virginia, USA
[22]School of Earth and Planetary Sciences, Curtin University, Perth, Western Australia, Australia
[23]School of Physics and Astronomy, University of Leicester, Leicester, UK
[24]Institut Chimie Physique, Centre National de la Recherche Scientifique, Université Paris-Saclay, Orsay, France
[25]Université de Lille, CNRS, INRAE, Centrale Lille, Université Artois, FR 2638-IMEC-Institut Michel-Eugène Chevreul, Lille, France
[26]Department of Mathematics, Physics, and Earth Science, Ehime University, Matsuyama, Ehime, Japan
[27]Department of Earth Science, Tohoku University, Sendai, Japan
[28]Materials Characterization Lab, The Pennsylvania State University, University Park, Pennsylvania, USA
[29]Institute for Chemical Research, Kyoto University, Kyoto, Japan
[30]Department of Advanced Materials Science, Kyushu University, Fukuoka, Japan
[31]The Ultramicroscopy Research Center, Kyushu University, Fukuoka, Japan
[32]School of Geology, Geography and the Environment, University of Leicester, Leicester, UK
[33]Division of Earth and Planetary Sciences, Kyoto University, Kyoto, Japan
[34]Center for University-Wide Education, Saitama Prefectural University, Saitama, Japan
[35]Centro de Química Estrutural, Institute of Molecular Sciences and Department of Chemical Engineering, Instituto Superior Técnico, Universidade de Lisboa, Lisbon, Portugal
[36]Jacobs Engineering, Dallas, Texas, USA
[37]The Hakubi Center for Advanced Research, Kyoto University, Kyoto, Japan
[38]CAS Key Laboratory of Mineralogy and Metallogeny/Guangdong Provincial Key Laboratory of Mineral Physics and Materials, Guangzhou Institute of Geochemistry, Chinese Academy of Sciences, Guangzhou, China
[39]School of Physics and Astronomy, University of Glasgow, Glasgow, UK
[40]Faculty of Engineering, Kindai University, Higashi-Hiroshima, Japan
[41]Marine Works Japan Ltd., Yokosuka, Japan
[42]École normale supérieure de Lyon, University Lyon 1, Lyon, France
[43]UTokyo Organization for Planetary and Space Science, University of Tokyo, Tokyo, Japan
[44]Institute for Molecular Science, UVSOR Synchrotron Facility, Okazaki, Japan
[45]Department of Earth and Planetary Sciences, Kyushu University, Fukuoka, Japan
[46]Japan Synchrotron Radiation Research Institute, Hyogo, Japan
[47]Institute of Materials Structure Science, High Energy Accelerator Research Organization, Tsukuba, Japan
[48]Department of Mechanical Engineering, Kanagawa Institute of Technology, Atsugi, Japan
[49]Department of Earth, Atmospheric and Planetary Sciences, Purdue University, West Lafayette, Indiana, USA
[50]Kochi Institute for Core Sample Research, X-Star, JAMSTEC, Nankoku, Kochi, Japan
[51]Research Organization of Science and Technology, Ritsumeikan University, Kusatsu, Shiga, Japan
[52]Department of Earth and Environmental Sciences, Nagoya University, Nagoya, Japan
[53]Department of Earth and Planetary Sciences, Hokkaido University, Sapporo, Japan
[54]Lunar and Planetary Laboratory, Department of Planetary Sciences, University of Arizona, Tucson, Arizona, USA
[55]ARES, NASA, Johnson Space Center, Houston, Texas, USA
***Correspondence**
Rhonda M. Stroud, School of Earth and Space Exploration, Arizona State University, Tempe, AZ, USA.
Email: rhonda.stroud@asu.edu

(Received 21 April 2023; revision accepted 01 January 2024)

Abstract–Transmission electron microscopy analyses of Hayabusa2 samples show that Ryugu organic matter exhibits a range of morphologies, elemental compositions, and carbon functional chemistries consistent with those of carbonaceous chondrites that have experienced low-temperature aqueous alteration. Both nanoglobules and diffuse organic matter are abundant. Non-globular organic particles are also present, and including some that contain nanodiamond clusters. Diffuse organic matter is finely distributed in and

around phyllosilicates, forms coatings on other minerals, and is also preserved in vesicles in secondary minerals such as carbonate and pyrrhotite. The average elemental compositions determined by energy-dispersive spectroscopy of extracted, demineralized insoluble organic matter samples A0107 and C0106 are $C_{100}N_3O_9S_1$ and $C_{100}N_3O_7S_1$, respectively, with the difference in O/C slightly outside the difference in the standard error of the mean. The functional chemistry of the nanoglobules varies from mostly aromatic C=C to mixtures of aromatic C=C, ketone C=O, aliphatic (CH_n), and carboxyl (COOH) groups. Diffuse organic matter associated with phyllosilicates has variable aromatic C, ketone and carboxyl groups, and some localized aliphatics, but is dominated by molecular carbonate (CO_3) absorption, comparable to prior observations of clay-bound organic matter in CI meteorites.

INTRODUCTION

The JAXA Hayabusa2 mission successfully delivered more than 5 g of material from the surface of Asteroid (162173) Ryugu to the Earth on December 6, 2020 (Tachibana et al., 2022). The samples were collected from two touchdown sites on Ryugu, separately stored in chambers A and C of the sample container. Chamber C samples may contain material excavated from some depth during an artificial impact experiment (Arakawa et al., 2020). A worldwide coordinated effort, organized into six focused Initial Analysis Teams began first-level characterization of the properties of the Ryugu regolith grains shortly thereafter, and continued measurements through May 2022. The analysis of Ryugu's organic matter (OM) was split primarily between two teams, the Soluble Organics Team addressing the soluble organic molecules (SOM) and the Organic Macromolecule Team addressing the acid-insoluble organic matter (IOM). A third team (Sand Team) focused on fine-grained mineralogy and the effects of space weathering. The major results from the Initial Analysis Core Team and subteams are summarized in a series of publications (Nakamura et al., 2023; Naraoka et al., 2023; Noguchi et al., 2023; Okazaki et al., 2023; Yabuta et al., 2023; Yokoyama et al., 2023). Additional reports from the Phase 2 curation team independently provided preliminary characterization of particle properties (Ito et al., 2022; Nakamura et al., 2022). These laboratory-based sample analyses confirmed a strong link between the returned Ryugu samples and the CI (Ivuna-like) class of carbonaceous chondrites. Although the Organic Macromolecule Team was not tasked with mineralogy studies and the Sand Team was not tasked with organic studies, asteroid regolith organic matter and nanoscale mineralogy are fundamentally interrelated. To address the nanoscale morphology and chemistry of the OM and its relationship to nanoscale mineralogy, we report here the results of transmission electron microscopy (TEM) studies from both the Organic Macromolecule and Sand teams.

In contrast with the expectations from remote spectroscopy measurements of the Ryugu surface (Kitazato et al., 2019, 2021; Sugita et al., 2019) that the samples would be heated and dehydrated, the returned Ryugu samples showed extensive hydration and little thermal alteration. Thermal and radiation processing of a thin surface layer through the collective processes known as space weathering (Pieters & Noble, 2016) may explain the discrepancy in part (Matsuoka et al., 2023). However, evidence for space weathering in the samples is limited (Noguchi et al., 2023). The interior OM is relatively pristine, except for variable levels of low-temperature aqueous alteration (Yabuta et al., 2023), with peak parent body temperature estimates as low as 40°C (Yokoyama et al., 2023). Because of the known provenance, lack of terrestrial atmosphere exposure, and minimal heating, Ryugu samples are among the most valuable representatives of organic matter from the early solar system and of the diversity of OM delivered to the surface of the early Earth.

Organic matter from asteroids and comets has been actively studied for several decades with ever more sensitive and powerful instrumentation (e.g., Alexander et al., 2017). The IOM from meteorites and cosmic dust consists of a macromolecular polymer comprising small aromatic domains, cross-linked with aliphatic chains. Carbon in all forms accounts for 3–4 wt% of the matrix of all carbonaceous chondrites (Alexander et al., 2017), with most of that carbon incorporated into the IOM, and <30% into SOM and minerals. Results from the Initial Analysis Chemistry team show that Ryugu contains to 4.63 ± 0.23 wt% carbon, with 3.08 ± 0.30 wt% in organic form; the excess carbon compared to carbonaceous chondrites such as Ivuna (CI) is attributed to abundant carbonate minerals (Yokoyama et al., 2023).

The overarching goals of meteoritic organic studies are to understand the nature of the OM delivered to the

[†]Deceased.

solar nebula from the interstellar medium and protosolar molecular cloud, as well as the subsequent nebular processing, accretionary history, and parent body processing. Ultimately, researchers of extraterrestrial organics seek to determine the conditions necessary for the formation of life and habitability, and their extent in time and space. The work reported here addresses the narrower question of how the OM in the Hayabusa2 samples compares and contrasts with OM from primitive carbonaceous chondrites, in particular CIs, as observed primarily by transmission electron microscopy in concert with other microanalytical techniques, including NanoSIMS, synchrotron X-ray absorption near edge spectroscopy, and atom probe tomography.

The two most common morphologies of the OM in primitive planetary materials are nanoglobules and diffuse intergranular matter. Nanoglobules are found in materials of cometary and asteroid origins (De Gregorio et al., 2013; Nakamura-Messenger et al., 2006) and are recognized by their spheroidal shapes, either hollow or solid, with typical diameters in the 100–1000 nm range. Nanoglobules with internal minerals have been reported (Hashiguchi et al., 2013) but are rare. The nanoglobules' spheroidal shape indicates a formation process that minimizes surface energy, possibly as discrete grains exposed to the molecular cloud or nebular ambient gas, or by precipitation of hydrophobic solids in C- or CO_2-rich fluids on asteroid parent bodies, or both. A single definitive pathway for their formation that explains the nanoglobules' full range of isotopic and chemical compositions has not emerged to-date, and multiple pathways may be required. The diffuse OM, in contrast to the nanoglobules, conforms to mineral grain surfaces, fills gaps between minerals, and can intercalate between silicate sheets in clay minerals (Garvie & Buseck, 2007; Le Guillou et al., 2014). Whereas the nanoglobules show evidence for minimization of surface area exposed to the matrix fluids or minerals, the diffuse OM is intermixed with the matrix minerals at the nanometer to sub-nanometer scale. The formation history of the diffuse meteoritic OM must therefore have been strongly affected by the extent and conditions of parent body hydrothermal alteration. Less common morphologies of OM are nonglobular particles, including extended vermicular shapes, and more compact, but non-spheroidal shapes, that is, dense, irregular OM.

Two forms of inorganic, elemental carbon are commonly found in primitive meteorites, nanodiamond and graphite. The most abundant is nanodiamond, at up to a few thousand ppm, matrix normalized. Nanodiamonds, which are distinct in origin from microdiamond that is found in more metamorphized meteorites, are co-located with the meteorite organics (De Gregorio et al., 2019; Garvie, 2010). They are known to carry isotopic signatures of formation in interstellar or circumstellar environments prior to the formation of the solar system (Lewis et al., 1987). However, the isotopically anomalous component is a trace constituent of the meteoritic nanodiamond isolates, and thus, only a minority of the nanodiamonds are required to have a presolar origin. Graphite grains that formed in presolar circumstellar outflows and core collapse supernovae occur in chondrites at ~ppm abundances, and can be identified by isotopic anomalies in C, N, O, and trace metals (Amari et al., 1990). Poorly graphitized carbon of solar system origin can also form by catalysis on metal and carbide grain surfaces at high temperature (Brearley, 2021; Ferguson et al., 2021) or thermal alteration of organic matter on asteroid parent bodies (Brearley, 1999).

Analyses of the functional group chemistry of OM at the sub-micron scale historically have relied on C, N, and O absorption spectroscopy with a scanning transmission X-ray microscope (Cody et al., 2008; Kebukawa et al., 2019; Le Guillou et al., 2014). Systematic differences in the average C K-edge spectra of the IOM from different classes of meteorites show relationships to parent body processing histories, with variations in the three most prominent functional groups, that is, aromatic carbon (C=C), ketone (C=O), and carboxyl (COOH). However, coordinated isotopic, X-ray spectroscopy and electron microscopy studies also show variations in chemistry at the sub-micrometer scale that are likely due to preserved signatures of nebular or molecular cloud processing. The IOM and Sand Team TEM studies of the Ryugu samples reported herein similarly show evidence for both extensive overprinting of hydrothermal alteration signatures and mineral–organic interactions, as well as preservation of some primordial nebular and presolar signatures.

METHODS

Ryugu regolith samples (Table 1) were provided by JAXA curation to the individual Initial Analysis team members as particles (A0108, C0109) or particle aggregates (A0104), focused ion beam (FIB) sections, and IOM residues (A0106, C0107). FIB sections (A0058-C2001-04, A0104-00200201, A0104-00200105, A0104-00200801) were prepared using an FEI Helios G3 Ga^+ FIB-SEM at Kyoto University and distributed to the University of Jena (A0058-C2001-04), the University of Hawai'i at Mānoa (A0104-00200201), and the US Naval Research Laboratory (NRL) (A0104-00200105 and A0104-00200801). For these sections, the particles were first coated with epoxy to protect any surface space weathering signatures, and then sectioned. A lift-out section of particle A0108 (A0108-3) was prepared for

TABLE 1. Summary of samples analyzed and respective preparation methods.

Sample	Preparation	Data in manuscript
A0108-3	Ga^+ FIB & Nanomill 1040, no electron beam exposure attachment after grid attachment, University of Tokyo	Figures 1a and 6
A0108-8	Sulfur embedding, ultramicrotomy, NRL	Figures 8 and 9
A0108-11	Ga^+ FIB of particle, no electron beam exposure after attachment, NRL	Figures 1g and 4a–e
A0108-28	Sulfur embedding, ultramicrotomy, NRL	Figures 2a–d and 3a
A0108-39	Sulfur embedding, ultramicrotomy, NRL	Figure 2e,f
C0109-2	Ga^+ FIB of particle pressed into Au mounts after NanoSIMS, no electron beam exposure after attachment, NRL	Figure 5
A0106	IOM residue, sulfur embedding and microtomy, NRL	Figures 11 and 12
C0107	IOM residue, sulfur embedding and microtomy, NRL	Figures 10 and 11
A0104-00200201	Epoxy coated, Ga^+ FIB with 2.5 kV electron beam exposure, Kyoto University	Figure 1d,e
A0104-00200105	Epoxy coated, Ga^+ FIB with 2.5 kV electron beam exposure, Kyoto University	Figure 7
A0104-00200801	Epoxy coated, Ga^+ FIB with 2.5 kV electron beam exposure, Kyoto University	Figure 1
A0058-C2001-004	Ga^+ FIB with 2.5 kV electron beam exposure, Kyoto University	Figures 1b and 3a
A0104-GLA0004	Xe plasma FIB sectioning of particle with 5 kV electron beam exposure, University of Glasgow	Figures 1f and 3b

scanning transmission X-ray microscopy (STXM) and TEM with a Hitachi FB-2100 FIB system and Fischione 1040 Nanomill at the University of Tokyo. Additional sample preparation was carried out at individual laboratories as noted. More details of the IOM team sample preparation can also be found in the supplementary materials in Yabuta et al. (2023).

Samples allocated to NRL as particles (sub-particles of A0108 and C0109) were prepared for coordinated STXM, nanoscale secondary ion mass spectrometry (NanoSIMS), and TEM by either sulfur embedding followed by ultramicrotomy with a Leica UC7 microtome or by FIB lift-out with an FEI Helios G3 Ga^+ FIB-SEM. Focused ion beam lift-out sections of subparticles of C0109 pressed into Au mounts and previously analyzed at the Carnegie Institution of Washington with NanoSIMS were also prepared. IOM residue samples (A0106 and C0107) allocated to NRL were prepared by sulfur embedding and ultramicrotomy. All NRL FIB preparation was carried out under protocols designed to limit the electron beam dose to the sample to preserve organic carbon functional chemistry (Bassim et al., 2012). X-ray absorption near edges spectroscopy (XANES) of the NRL samples was carried out at the Advanced Light Source Beam line 5.3.2.2 prior to TEM analysis to eliminate the chance of artifacts in the STXM data due to the alteration of the functional chemistry in the TEM.

The TEM analyses performed at NRL were carried out with two microscopes: a JEOL 2200FS operated at 200 kV for bright-field (BF) TEM image imaging and a Nion UltraSTEM 200-X operated at 60 kV for annular dark-field (ADF) and BF imaging, electron energy loss spectroscopy (EELS), and energy-dispersive X-ray spectroscopy (EDS) of most samples. The UltraSTEM was equipped with a windowless, 0.7sr Bruker Xflash 100 silicon drift detector (SDD), and a Gatan Enfinium ER energy loss spectrometer. Simultaneous EDS and EELS spectrum images were recorded with Gatan Digital Micrograph software. Higher resolution EDS spectrum images were recorded with Bruker Esprit 1.92 software. UltraSTEM analyses of sample A0104-00200105 were performed at 200 kV due to the primary allocation of this sample for fine-scale mineralogy studies.

TEM studies of sample A0058-C2001-04 were performed at the University of Jena with an FEI Tecnai G2 FEG TEM, operating at 200 kV. Conventional BF, DF, and high-resolution (HR) images and selected area electron diffraction (SAED) patterns were acquired using a 2K CCD camera (Gatan Ultrascan). Z-contrast and low magnification STEM images were recorded using a high-angle ADF (HAADF) STEM detector (Fischione) at camera lengths of 100 mm and 5.1 m, respectively. An Oxford Instruments X-MaxN80^T SDD EDS system was employed for the quantification of chemical compositions and elemental mapping of phases. Electron energy loss near-edge spectra (ELNES) were acquired with a post-column Gatan Imaging Filter (GIF) Quantum. The ELNES measurements were carried out in diffraction mode at a camera length of 200 mm and an energy resolution of 0.8 eV (defined as full width at half maximum height of the zero-loss peak). In order to minimize electron beam damage, all measurements with performed with a Gatan liquid nitrogen holder that cooled the samples down to about 110 K.

TEM studies of sample A0104-00200201 were performed at 300 kV with the FEI Titan G2 dual aberration-corrected analytical (S)TEM at Advanced Electron Microscopy Center (AEMC) at the University of Hawai'i at Mānoa. High-angle ADF HAADF images and nanobeam diffraction patterns were collected with a

Gatan Ultrascan 1000 camera. EDS data were obtained with a 0.16 sr EDAX Genesis SDD. Hyperspectral element maps were collected at the Molecular Foundry, Lawrence Berkeley National Laboratory using an 80–300 kV TitanX ChemiSTEM with a 0.7sr Bruker EDS system (0.7sr) of four windowless SDDs and Bruker Esprit 1.9 software.

TEM studies of sample A0104-GLA0004 were performed in the School of Physics and Astronomy, University of Glasgow, United Kingdom. Lamellae ~15 × 10 × 0.1 μm in size were cut and extracted from the outer surfaces of ~100 μm-sized Ryugu grains with an FEI Helios Plasma FIB. The lamellae were initially characterized with BF TEM imaging and SAED using an FEI Tecnai T20 TEM operated at 200 kV. Subsequently, HAADF images and EDS and EELS maps were collected from areas of interest using a JEOL ARM200F cold field-emission TEM operated at 200 kV. For chemical analysis, the microscope is equipped with a Bruker XFlash 60 mm^2 EDS detector and a Gatan Quantum electron energy loss spectrometer.

We studied Ryugu OM both in situ with preserved petrographic context in FIB lift-out sections and in ultramicrotome sections, and ex situ as ultramicrotome slices of demineralized, acid-resistant residues, that is, IOM. Each preparation was intended to facilitate measurements of specific features of the OM. The FIB sections are the only preparation compatible with atom probe tomography, and best preserved the petrographic context and water-soluble components. However, the overlap of materials within the thickness of the FIB sections obscured some nanometer-scale features such as nanodiamonds and organic–mineral interfaces in TEM and XANES measurements. Ultramicrotome sections provided the thinnest observable areas, enabling easier TEM and XANES observation of nanodiamonds and interfaces between OM and minerals, but suffered some disruption of the petrography due to ultramicrotome blade chatter and potential loss of any water-soluble components, such as halide crystals or the most highly soluble organics, due to the use of a water bath for the microtomy. The ultramicrotome sections of extracted IOM best enabled representative bulk measurements of the elemental composition of the OM due to the removal of the majority of minerals, but some nanoparticulate minerals were retained and some soluble components were removed by the sample preparation. The use of the full range of sample preparation methods helped ensure that the resultant data provided a more comprehensive understanding, not subject to a common set of artifacts and methodological biases.

Electron microscopy and synchrotron X-ray absorption near edge spectroscopy were both important components of the initial analyses. With the current STXM instrumentation, C XANES data at 50 nm spatial resolution and 0.1 eV energy resolution are routinely possible. The soft X-ray beam of the polymer STXM beamlines is below the energy threshold for causing displacement damage to the IOM, but ionization damage can still occur (Coffey et al., 2002), particularly for aliphatic-rich polymers. Furthermore, depending on the beam current and scan rate, thermal damage to the IOM can occur. In contrast, traditional TEM operating voltages for planetary material studies of 200 or 300 kV are in the range for both radiolysis and displacement damage, which significantly reduces the utility of ambient temperature TEM for IOM studies other than morphological studies due to the need to use extremely low-dose conditions to avoid major alterations to the elemental and functional group chemistry. However, low-voltage scanning transmission electron microcopy (STEM) at 60 or 80 kV eliminates the displacement damage for the major IOM elements (C, N, O, S) besides H, and makes it possible to use STEM-based energy-dispersive X-ray spectroscopy for the elemental composition determination. With a cold-field emission electron source, energy resolutions of 0.3 eV for ELNES, the electron microscopy technique analogous to XANES, are possible at resolutions down to sub-angstrom if carried out with an aberration-corrected STEM on appropriately thin samples. Such "gentle STEM" measurements have proven an important resource for determining the elemental and functional group chemistry of features of the IOM at spatial scales inaccessible with current STXM instruments (Stroud et al., 2021; Vollmer et al., 2014). The trade-off for using lower voltage in the electron microscope is the need for thinner samples to avoid multiple scattering effects; 0.1–50 nm is suitable for organic samples at 60 kV. While this is helpful for analyzing the features that are inherently at the single atom to few nm scale, such as nanodiamonds and mineral–organic interfaces that are inaccessible to XANES, it complicates 1:1 comparison of STXM and STEM data, because the scattering length of the soft X-rays constrains the ideal thickness of the IOM samples for XANES to 50–200 nm; samples thinner than 50 nm generally provide poor signal/noise for typical measurement conditions. For working with thicker samples or direct comparison with XANES, higher voltage TEM measurements with a liquid nitrogen cold stage, such as for sample A0058-C2001-04, provide an alternative to low voltage for limiting the electron beam induced damage. For this study, we performed STXM before STEM measurements on exactly the same sample whenever possible, to ensure the greatest fidelity of the carbon functional chemistry at the highest spatial resolution. The use of multiple electron microscopy methods on the variously prepared samples, in conjunction with coordinated XANES measurement,

provides the greatest assurance in the reliability of the results compared to conventional TEM or XANES alone.

RESULTS

Nanoglobules

Nanoglobules are common in FIB sections of Ryugu particles, as observed with TEM and STEM imaging (Figure 1). Most nanoglobules are between 50 and 500 nm in diameter, with some as small as 10 nm, and some larger than 2000 nm. They occur in solid (Figure 1a,b), hollow (Figure 1f), and multi-rimmed forms (Figure 1c,f). Some are isolated individual grains embedded in phyllosilicates (Figure 1a), while others occur in clusters (Figure 1f,g). Many of the nanoglobules have abrupt boundaries with the surrounding phyllosilicates that spatially conform to the nanoglobule surfaces (Figure 1d). Other nanoglobules have diffuse boundaries and infiltrate the surrounding phyllosilicates (Figure 1g, upper and right nanoglobules).

The interface between smaller nanoglobules and the surrounding phyllosilicates is easiest to image in ultramicrotome sections (Figure 2), which are generally thinner (30–70 nm) than the FIB sections (100–150 nm). In many cases, the phyllosilicates literally surround the nanoglobules as a conformal coating (Figure 2a,c), whereas in other cases (Figure 2e), no distinct relationship between the nanoglobules and phyllosilicates is observed.

The elemental and functional chemistry of the nanoglobules is heterogenous among different globules, and also occasionally even within an individual nanoglobule (Figure 3). EELS measurements of many A0108 microtomed globules show predominantly aromatic C bonding. Whereas other globules in both microtomed and FIB prepared samples show more complex chemistry. The EELS data from a microtomed double-walled nanoglobule from C0107 IOM show mixed aromatic, ketone, and carboxyl functional chemistry, consistent with the published XANES spectra from the same sample (Yabuta et al., 2023). The two solid nanoglobules in A0058-C2002-04 have prominent peaks corresponding to aromatic C at 285 eV and aliphatic carbon at 287.5 eV, with a weaker ketone feature at 286.5 eV. The multi-rimmed nanoglobule (A0104-GLA0004) shown in the right side of Figure 3b shows more abundant N in the interior.

Diffuse Carbon

Diffuse carbon, defined here as organic carbonaceous matter without clear particulate boundaries, is abundant throughout the fine-grained Ryugu matrix (Figure 4). It is difficult to directly image the diffuse carbon in FIB sections with TEM and STEM due to the small feature size and to intermixing with higher contrast materials (Figure 4a,c,e) such as Mg-phyllosilicates, magnetite,

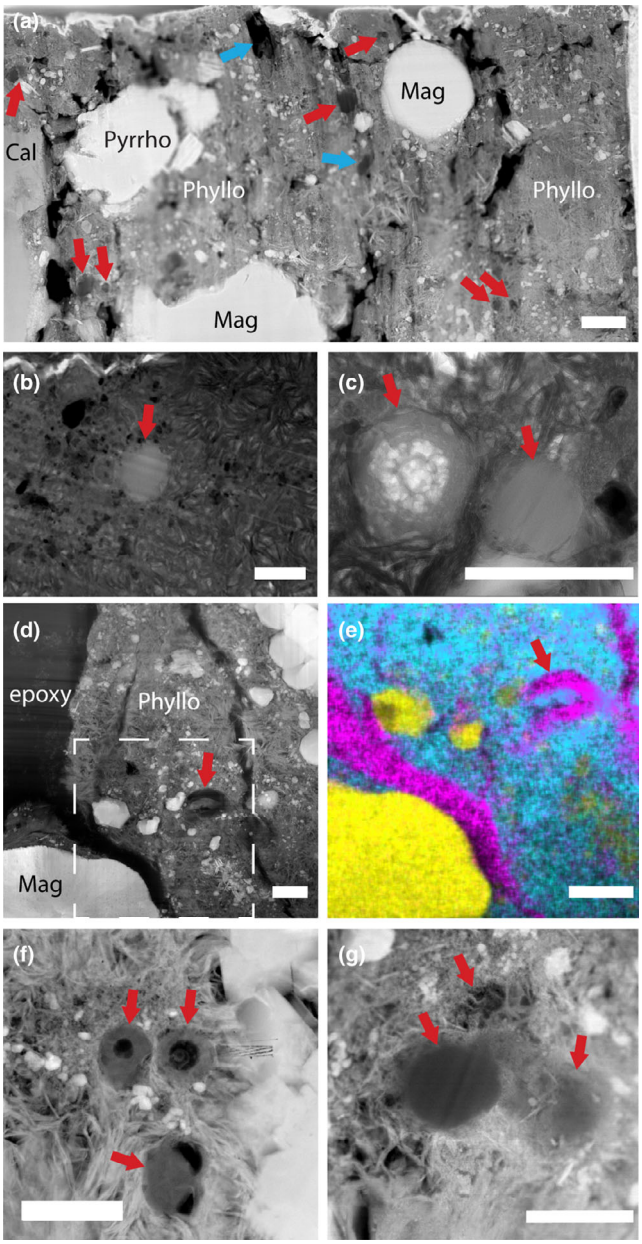

FIGURE 1. Transmission electron microscopy images of Ryugu nanoglobules in situ. Red arrows indicate the nanoglobule locations. Blue arrows indicate nonglobular particulate carbon. All scale bars are 500 nm. (a) HAADF of A0108-3. (b) BF TEM of A0058-C2001-04. (c) BF TEM of A0104-00200801. (d) HAADF of A0104-00200201 solid and multi-rimmed globules (e) EDS composite map of O (cyan), C (magenta), and S (yellow) overlay on HAADF image of A0104-00200201. (f) HAADF image of A0104-GLA0004 with compound globules. (g) HAADF of three nanoglobules in A0108-11 intersected by the FIB cut at different depths. The left globule has well-defined boundaries with the surrounding phyllosilicate, but the upper and right nanoglobules show carbon extending into the phyllosilicates.

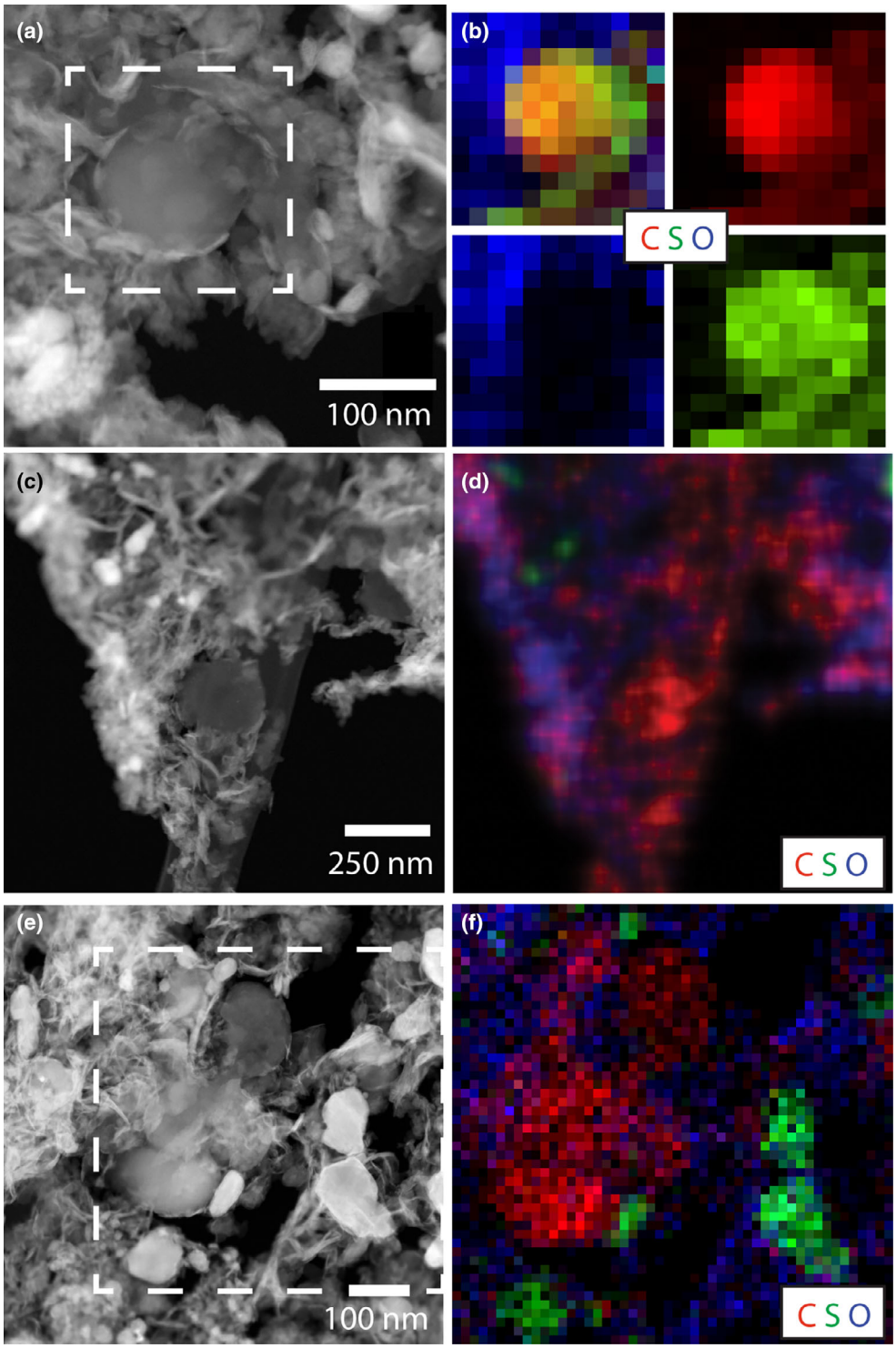

FIGURE 2. HAADF images and EDS elemental composite maps (C (red), S (green), O (blue)) of nanoglobules in microtome sections of Ryugu particles. (a) HAADF of a sulfur-rich nanoglobule with attached conformal phyllosilicates from A0108-28. The dashed line box indicates the ROI for a simultaneous EDS-EELS spectrum image. (b) EDS composite of the A0108-28 nanoglobule. (c) HAADF image of a heteroelement-poor nanoglobule, and a nonglobular carbon particle. (d) EDS composite map of (c). (e) HAADF image of clustered nanoglobules in A0108-39. The dashed line box indicates the ROI for a simultaneous EDS-EELS spectrum image. (f) Composite EDS map of the A0108-39 nanoglobule cluster.

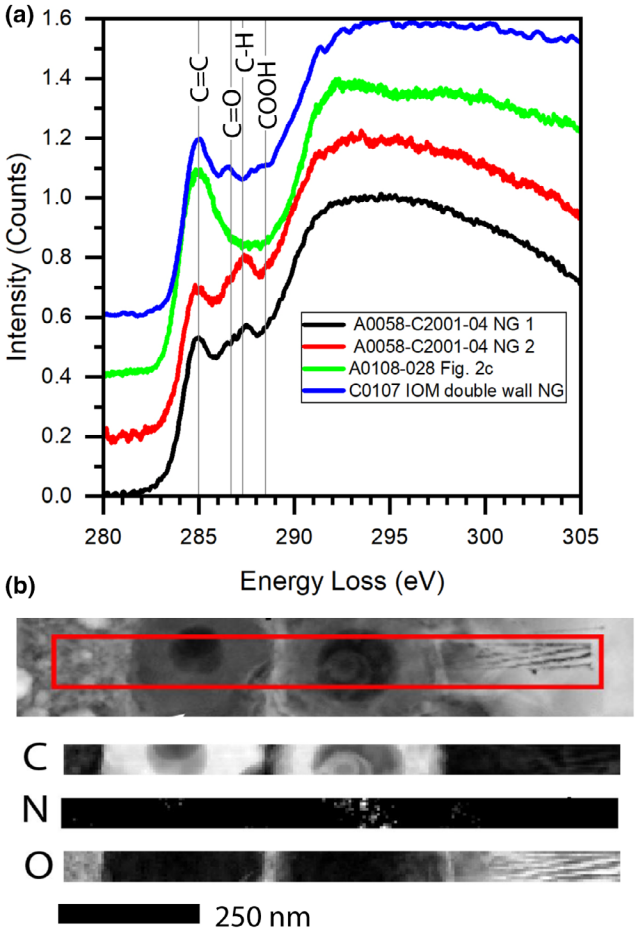

FIGURE 3. Electron energy loss near-edge spectroscopy (a) of nanoglobules from A0058-C2001-04, A0108-028, and C0107 IOM, and energy filtered imaging (b) of nanoglobules from A0104-GLA0004 illustrating diversity in functional chemistry. Many nanoglobules predominantly contain aromatic C, while others have mixed aromatic, ketone, aliphatic, and carboxyl chemistries. Some globules show internal variations in the N/C that suggest formation from multiple reservoirs.

pyrrhotite, and carbonates. However, the diffuse carbon is easily observed in EDS maps (Figure 4b,d,f), as well as in atom probe tomography (APT) data, where it can be seen to infiltrate between layers of phyllosilicates and to form coatings on sulfides and the insides of pores. The APT measurements indicate that some of the diffuse carbon is in the form of discrete 5–7 nm subrounded irregular shaped inclusions within phyllosilicates and near pore space (Daly et al., 2022).

The diffuse carbon can constitute a major fraction of the total materials present even when it does not provide sufficient contrast for direct imaging. For example, the BF STEM image (Figure 5a) of a FIB section of particle C0109-2 shows a matrix of Mg-rich phyllosilicates with a submicron pyrrhotite and many nanoscale Fe,Ni sulfides, with no visible distinct carbonaceous particles. The contrast in C XANES images (Figure 5b) from the section is dominated by the C in the protective strap, and the higher density Au substrate, obscuring the C intensity in the sample. However, the XANES spectra from the section normalized to the vacuum intensity show strong absorption at the C edge. The extracted sum spectrum over μm^2 scale areas (Figure 5d red outlined region of interest (ROI) is dominated by a CO_3 feature at 290.4 eV, with three additional major peaks corresponding to aromatic C=C (285 eV), aromatic ketone C=O (286.7 eV), and carboxyl (288.5 eV; Figure 3e). Over scales of a few 10s of nm, the relative intensities of the aromatic C, ketone, and carboxyl peaks vary significantly, and other peaks such as an aliphatic C-H (287 eV) peak occasionally occur. The C/Si elemental ratio in the section can be measured with STEM EDS, for example, in Figure 5b the ROI outlined in white has a nominal C/Si of 0.8, which includes a surface carbon contamination layer from the FIB preparation, estimated at 20% of the total C counts. Accounting for the surface contamination, the sample C/Si ratio in this ROI is ~0.6, in good agreement with the bulk values of 0.3 mass ratio (~ 0.65 atom ratio) obtained by Yokoyama et al. (2023). For other FIB sections from the same particle without resolvable discrete carbonaceous particles, the C concentration was found to vary from region to region by ~20%, due to intrinsic heterogeneity. Thus, the diffuse carbon appears to constitute the majority of the organic carbon, with the more readily imaged large nanoglobules accounting for <20%.

Vesicle-Trapped Carbon

The FIB-prepared samples allowed for the observation of another type of carbon, namely carbon trapped in vesicles in secondary minerals. In an FIB section of A0108-3 (Figure 6), DF STEM imaging revealed a large calcite grain that contains abundant vesicles, some of which are hollow, and some containing a mixture of nanoscale minerals and diffuse carbon. Because the depth of the FIB section slice compared to the exterior surface of the original calcite grain surface in the viewing direction is unknown, a section that samples surface cavities can be difficult to distinguish between a section that samples fully interior vesicles. We interpret the features in this section as fully interior vesicles because the calcite has well-defined faceted grain boundaries on two sides with many of the vesicles occurring at distances from the grain edges greater than the roughness of the grain boundaries, and some of the vesicles show empty interiors, except for small precipitate minerals on the edge of the vesicles. The minerals and organic matter present in the vesicles, therefore, represent the products of asteroidal fluids trapped during the

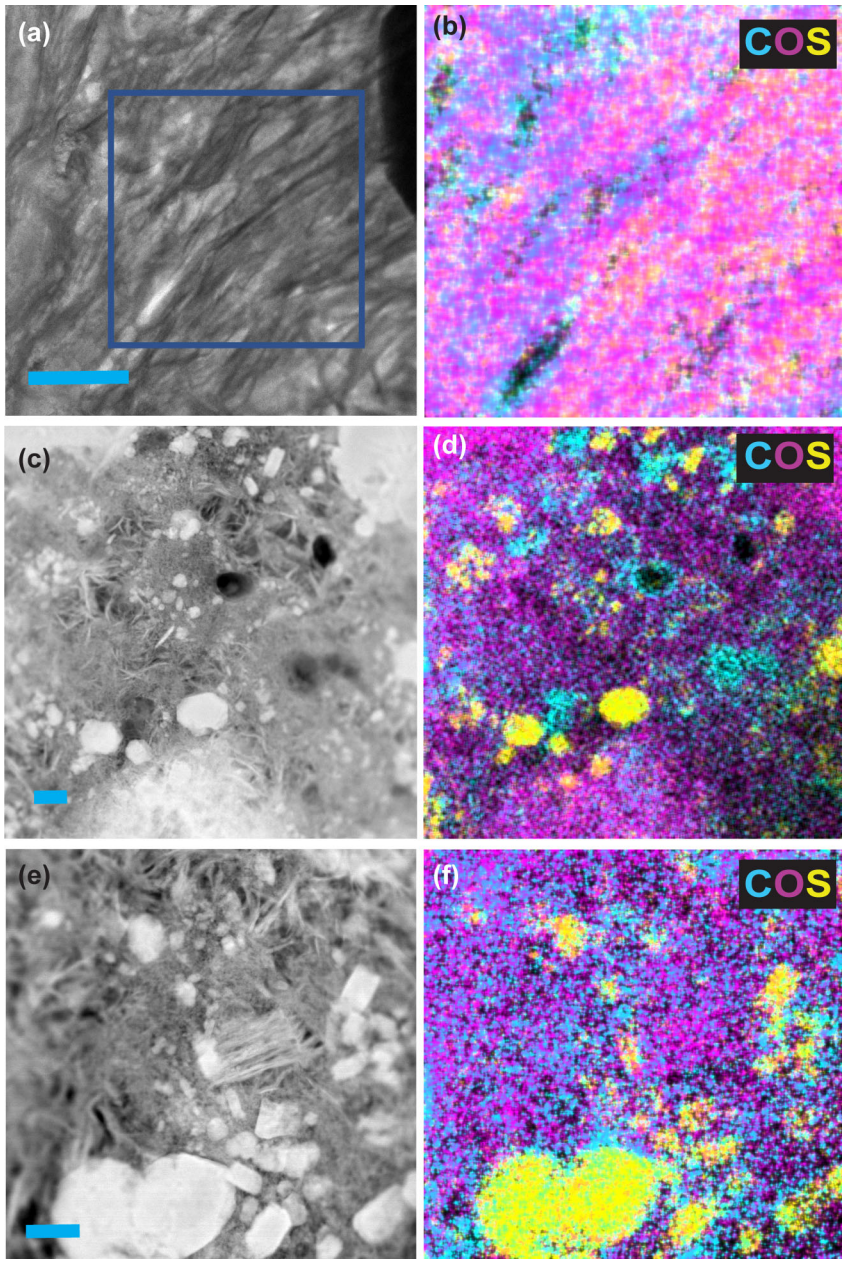

FIGURE 4. STEM BF (a) and HAADF (c, e) images and EDS composite maps (C) (cyan), O (magenta), S (yellow)) of diffuse carbon in Ryugu particle A0108-11 FIB sections. All scale bars are 200 nm. (a, b) Diffuse carbon interspersed in phyllosilicates sheets. (c, d) Diffuse carbon coating and filling pores in phyllosilicates. (e, f) Diffuse carbon coating two adjacent Fe sulfide grains and filling pore space in phyllosilicates.

formation of the carbonate. STEM-EDS mapping shows these include diffuse carbon, phyllosilicates, and sulfides (Figure 6c). STEM-EELS of the OM indicates that it is amorphous, distinct from the clear calcite signature of the host carbonate (Figure 6e,f).

Vesicles containing remnants of asteroidal C-rich fluids were also found in an ~0.5 μm pyrrhotite grain in a FIB section of grain A0104-00200801 (Figure 7). The vesicles were ~1 nm to 50 nm in diameter, and show excess C and O compared to the host pyrrhotite in STEM-EDS maps. In addition, low-loss EELS measurements of the vesicles show excess intensity between 5 and 7 eV and at 13 eV from C-, H-, and O-rich species. The EELS spectra obtained at the C K-edge (not shown) are consistent with C-O species, but are too noisy for a definitive bonding identification.

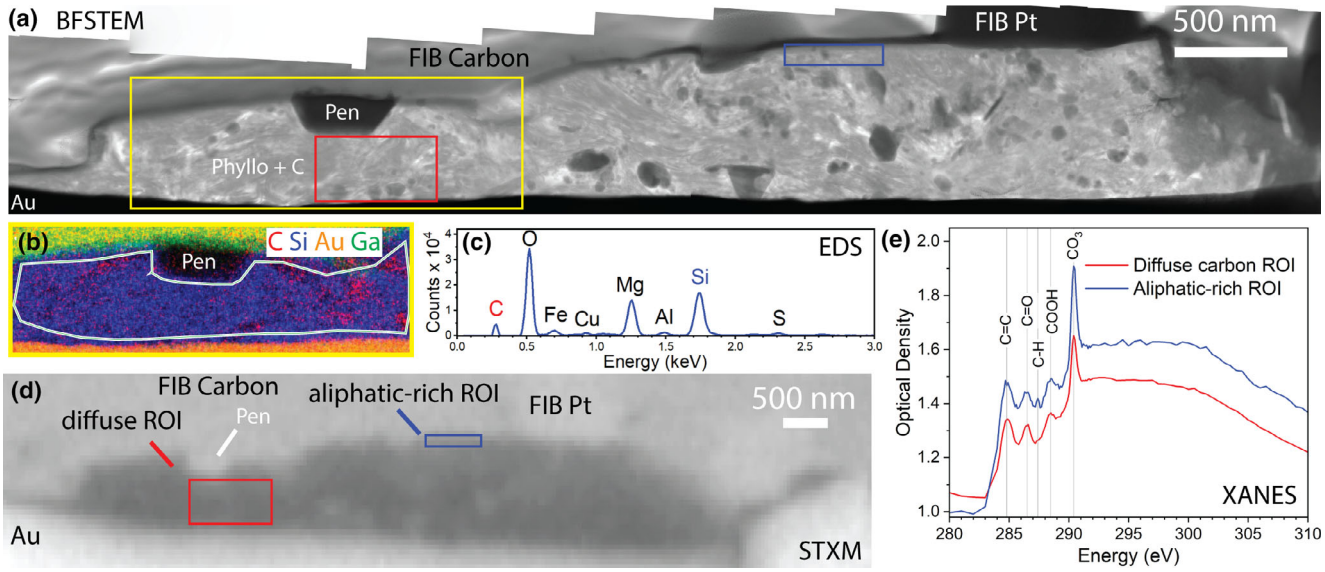

FIGURE 5. STEM and STXM analyses of diffuse carbon in a FIB section of particle C0109-2. (a) BF STEM mosaic image revealing Fe, Ni sulfides in a phyllosilicate matrix. The labels Pen and Phyllo indicate pentlandite and phyllosilicates, respectively. The yellow rectangle indicates the ROI for a STEM-EDS spectrum image. The red and blue rectangles are ROIs for the XANES sum spectra. (b) Composite EDS map (Red = C, Blue = Si) of the yellow rectangle ROI in (a). The white outline indicates the boundary of the region of the extracted sum spectrum in (c) which excludes the pentlandite grain. (c) Extracted EDS sum spectrum of the phyllosilicate and diffuse carbon region, with a calculated C:Si molar ratio of 0.8. This ratio includes some surface C contamination and is thus an upper bound for this ROI. (d) STXM image of the C0109-2 FIB section at 288.9 eV. (e) Extracted C XANES spectra of typical diffuse C with a prominent absorption peak at 290.4 eV from red box ROI in (d) and a region of enhanced aliphatic C at 287.4 eV (blue box) in (d).

Nanodiamonds

Nanodiamonds are easiest to observe in ultramicrotome sections due to their small size. We used STEM-EELS spectrum imaging to locate them in sections of particles from both chamber A and chamber C. The nanodiamonds occur in clusters embedded in amorphous carbon and are individually 1–5 nm in diameter. Although their greater density compared to the surrounding amorphous carbon makes it possible to discern them by medium-angle annular dark-field (MAADF) imaging once located by EELS (Figure 8c), the subtle intensity difference is easily overwhelmed by the mineral–OM contrast in the larger scale images (Figure 8a,b). In EDS spectra, the nanodiamonds appear to contain more N than the surrounding amorphous carbon (Figure 8e).

Dense, Irregular Organic Matter

The final morphological category of OM we observed in situ has well-defined boundaries, but lacks the compact spherical shape of the nanoglobules, and thus we refer to it as dense, irregular OM (Figure 9). Sometimes, the dense irregular OM appears to worm-shaped (vermicular). In other cases, it is more equiaxed in aspect ratio, but has ruffled edges inconsistent with surface area minimization. Some of the dense, irregular OM might be nanoglobules that fractured on Ryugu or during laboratory sample preparation. Figure 9a shows a large vermiform OM particle from sample A0108-11, which was present in several microtome sections, including a thicker section prepared for NanoSIMS measurements shown in fig. S7 of Yabuta et al. (2023), in which the same particle was classified as a 2-μm hollow nanoglobule, with D and ^{15}N enrichments. The functional chemistry and elemental composition of the dense, irregular OM is variable at scales of 20 nm. The vermiform OM/fractured nanoglobule in Figure 9a is aromatic in functional chemistry, with low N and O, and S below detection limit. Panels C–G of Figure 9 show two ~100 nm scale nanoglobules, and a 400-nm long vermiform particle. The EDS data (Figure 9d) show that the vermiform particle is rich in N at the top (ROI1) and higher in O in the middle and lower region (ROI2). This difference is reflected in the EELS spectra (Figure 9g) in which ROI 1 shows a broadening of the aromatic peak to include C=N as well as C=C, whereas ROI 2 shows a narrower aromatic peak C=C, with increased intensity at the carboxyl peak (COOH) accounting for the increased O in the EDS signal. The upper nanoglobule (ROI3) is depleted in N and S compared to the other OM, shows the narrowest aromatic C=C peak, with a small shoulder at the carboxyl position. The lower nanoglobule is relatively

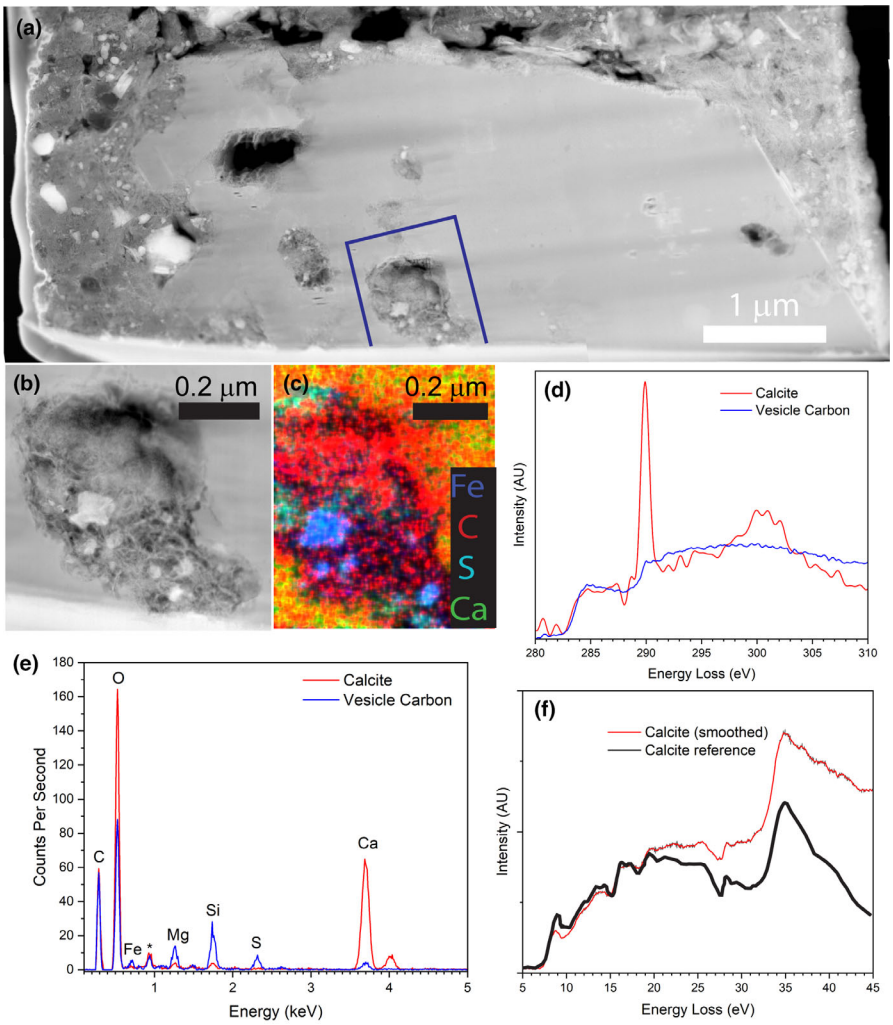

FIGURE 6. (a) HAADF mosaic image of a calcite grain in a FIB section of A0108. The blue outline indicates ROI shown in (b). (b) HAADF of a vesicle in the calcite. (c) EDS composite net count map (Fe (blue), C (red), S (cyan), Ca (green)) of the vesicle, with 3 pixel smoothing. (d) Extracted EDS spectra of the calcite (red) and diffuse C and nanominerals (blue) in the vesicle, normalized to C counts. (e) C core-loss EEL spectra of the calcite and amorphous carbon in the vesicle. (f) Comparison of the low-loss EEL spectrum of the Ryugu calcite to a reference spectrum from naturally formed calcite (Srot et al., 2013).

enriched in N and S, and shows multiple peaks, including a possible aliphatic (C-H_n) peak.

Morphology in Ultramicrotomed IOM

Ultramicrotome slices of the extracted IOM allow for large areas of OM to be imaged and analyzed (Figure 10). Much of the IOM is "fluffy," that is, it appears to be porous and irregularly shaped, with a feature size of a few nms, and may constitute a portion of what falls under the category of diffuse carbon in the FIB sections. Nanoglobules in multiple forms, that is, solid, and hollow, single-walled and multiwalled, fractured, isolated, and in connected clusters are also readily observed. Globules <200 nm are much more easily observed in the IOM sections as well. In EDS maps, the elemental composition shows variations in the C, N, and O and S abundance at the few nm scale. The STEM-EELS data also show variation in the functional chemistry at this scale, with both aromatic C=C dominated and mixed functional group chemistries, including some particles with chemistries that are not observed at the bulk scale. Most significantly, the CO_3 carbonate feature so prominent in the FIB section diffuse carbon and detected in the phyllosilicate clay flakes in ultramicrotome sections, is completely absent.

The IOM extracts allowed individual particle and large area average measurement of the N/C, O/C, S/C, and Si/C atom ratios, as summarized in Figure 11. Individual particles show N/C values of up to 0.09, but on average O is more abundant than N. The average compositions of the A0106 and the C0107 IOM obtained

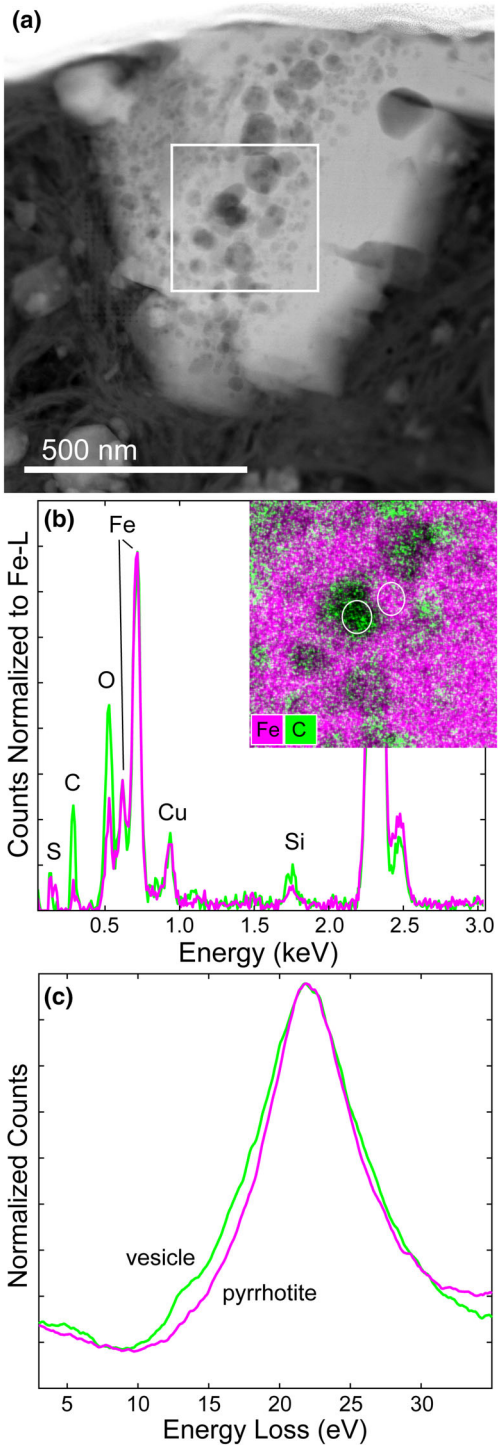

FIGURE 7. (a) HAADF image of an FIB section of A0104-00200801 showing a 0.5 μm pyrrhotite grain with abundant vesicles. (b) Comparison of the EDS spectrum normalized to Fe-L counts of an ROI with a closed vesicle to an adjacent region of the host pyrrhotite, as indicated on the inset composite Fe,C EDS map of the outlined ROI in (a). The vesicle contains abundant C and O absent from the pyrrhotite. (c) Low-loss EELS of the pyrrhotite and closed vesicle after deconvolution of the zero loss peak. The vesicle shows extra intensity between 5 and 7 eV and at 13 eV associated with carbon, oxygen, and OH. Contributions from Ga plasmons at the 16 eV feature can be ruled out by their absence in the adjacent pyrrhotite.

from EDS were $C_{100}N_{3\pm0.6}O_{9\pm1}S_{1\pm0.06}$ and $C_{100}N_{3\pm0.4}O_{7\pm0.5}S_{1\pm S0.1}$, respectively, with the uncertainty reported as the SE of the mean. These measurements exclude all visible retained mineral nanoparticles. Such phases include sulfides, SiC, and spinels with variable Fe, Cr, Al, and Mg, as revealed in the EDS maps.

In some cases, the physical relationship between the IOM and the retained nanoparticles can provide constraints on the origin and processing history of the IOM. For example, Figure 12 shows a copper sulfide surrounded by aromatic OM. The sulfide is most likely a product of parent body aqueous alteration, and the aromatic IOM coating associated with it is therefore most likely also a product of parent body alteration.

DISCUSSION

General Features

In sum, the data reported herein provide a comprehensive overview of the morphological and elemental diversity of organic matter within the Hayabusa2 samples. Ryugu regolith OM shows all of the same major morphological categories as does primitive carbonaceous chondrite meteorite OM, including nanoglobules, dense irregular OM, diffuse carbon, and nanodiamonds. Furthermore, we observed all of these OM features in particles from both Chamber A and Chamber C, with no statistically significant differences in morphology or composition, other than a possible small increase in the O/C the IOM from chamber A. Large veins of OM, occasionally observed in carbonaceous chondrites (e.g., Alexander et al., 2017; Floss et al., 2014; Le Guillou et al., 2014) were not observed in particles from either chamber in our study, but this could be due to the small aggregate particles allocated for these initial analyses. Larger veins could be present in larger coherent particles. The Ryugu OM functional chemistry is dominated by four main groups: aromatic (C=C), ketone (C=O), carboxyl (COOH), and carbonate (CO_3), with lesser amounts of aliphatics (C-H_n). The aliphatic content of the Ryugu IOM observed by TEM EELS and STXM varies among particles, but appears to be higher than in Murchison IOM measured under similar conditions at NRL, which is consistent with bulk IOM measurements showing a greater aliphatic relative abundance for CIs than CMs (Cody & Alexander, 2005). Aliphatic-rich OM

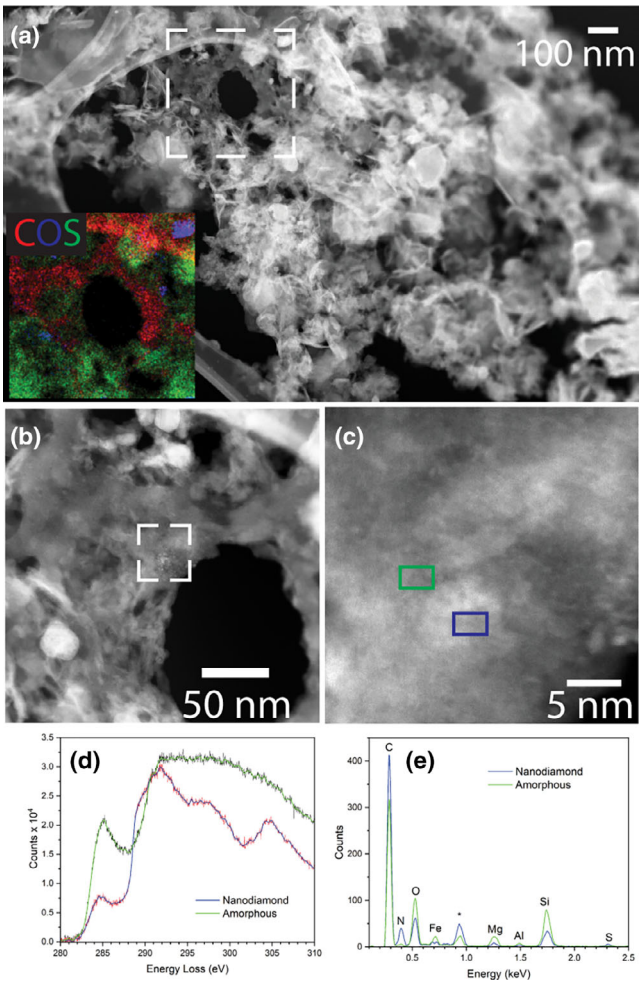

FIGURE 8. (a) HAADF STEM overview of a microtome section of particle A0108-08 with inset composite EDS map (C [red], S [green], O [blue]) of a nanodiamond-rich region indicated with dashed white box. (b) HAADF image at higher magnification of the upper left corner of the nanodiamond-rich area. The white dashed box indicates the ROI for a simultaneous EDS-EELS spectrum image. (c) MAADF image of the spectrum image ROI. The denser nanodiamonds are brighter than the surrounding amorphous C. The blue and green rectangles indicate ROIs for extraction of sum spectra from nanodiamond and amorphous carbon regions, respectively. (d) EEL spectra of a nanodiamond and the adjacent amorphous C. (e) Extracted EDS data from the nanodiamond and amorphous carbon, normalized to the C intensity. The amorphous C shows greater amounts of O and Si, whereas the nanodiamond has greater N.

was also reported by Ito et al. (2022). Ryugu nanoglobules occur in both predominantly aromatic and "IOM-like," that is, mixed aromatic, ketone, aliphatic, and carboxyl functionality, as does the dense irregular OM. The diffuse carbon is dominated by molecular carbonate, but has variable amounts of the other groups.

Pervasive but Heterogenous Hydrothermal Alteration

The mineral–organic morphological features and spatial relationships we observed indicate that most of the OM is affected by one or more episodes of hydrothermal alteration. The carbonaceous species trapped in vesicles in secondary minerals, including calcite and pyrrhotite, represent early stages of the alteration, potentially preserving remnants of the asteroidal fluids, or at least subsequent products. In addition to the two examples of volatile-bearing inclusions reported herein, examples of such inclusions in larger pyrrhotite grains were identified through synchrotron X-ray tomography methods (Nakamura et al., 2023). This confirms that these features are not constrained to a single Ryugu particle, but instead represent a more widespread alteration process in the Ryugu regolith or prior parent body.

The IOM isolates from both chambers retained significant populations of inorganic nanoparticles (2–200 nm), including spinels with Mg-Al, and Cr-Fe-rich compositions, sulfides rich in Fe, Ni, Zn, and Cu, and presolar SiC. These grains were excluded from the STEM-EDS compositions but could contribute to SIMS-based elemental analysis of the IOM as most are too small to be resolved in NanoSIMS data. The Cr-Fe spinel and metal sulfide grain populations are sensitive to thermal and aqueous parent body processing, and population studies in the future might provide constraints on Ryugu alteration conditions.

Diverse Features of Nanoglobules Indicate Diverse Origins

Based on the diversity of Ryugu nanoglobules, the formation history of these objects is varied rather than constrained to a single process. Nanoglobules with well-defined exterior boundaries and conformal phyllosilicate

FIGURE 9. 60 kV STEM-EDS-EELS analysis of dense irregular OM in microtomed sections pf particle A0108-11. (a) False color HAADF image of vermicular organic matter (red). (b) EDS and inset C EELS from the vermicular carbon. (c) HAADF image of a microtome section of particle A. The white dashed box defines an ROI for a simultaneous EELS-EDS spectrum image. Two spectrum images were recorded, one with low-loss EELS and one at the C K-edge. (d) Composite EDS map (C [red], N [green], O [blue]) revealing four ROIs of the organic matter with distinct elemental composition. (e) Extracted low-oss EELS image at 5 eV, showing the distribution of π-bonded carbon (white). (f) Extracted spectra of the four ROIs from the EDS SI. (g) Extracted spectra from the simultaneously acquired C K edge SI. The variation in N and O observed in the EDS data is correlated with the relative intensities of the N and O functional groups. Although the S content detected in the EDS also varies, the S functional group absorption is too weak to detect in the EELS data.

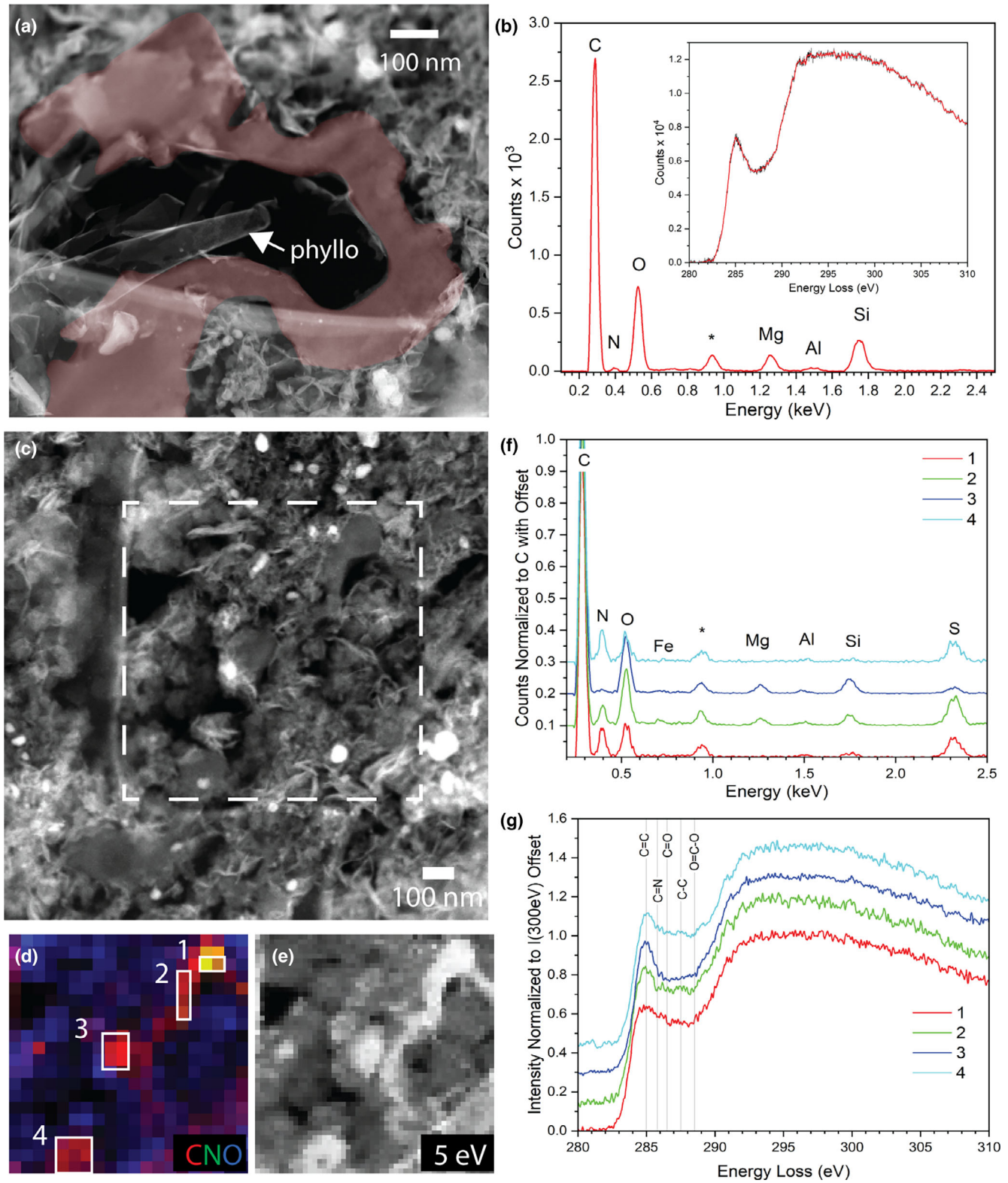

coatings formed coincident with or prior to hydrous alteration of the primary silicates. These nanoglobules are thus either nebular or proto-solar molecular cloud products, or products of parent body organic reactions at temperatures below the melting temperature of water ice, perhaps driven by melting of CO_2 ice. The

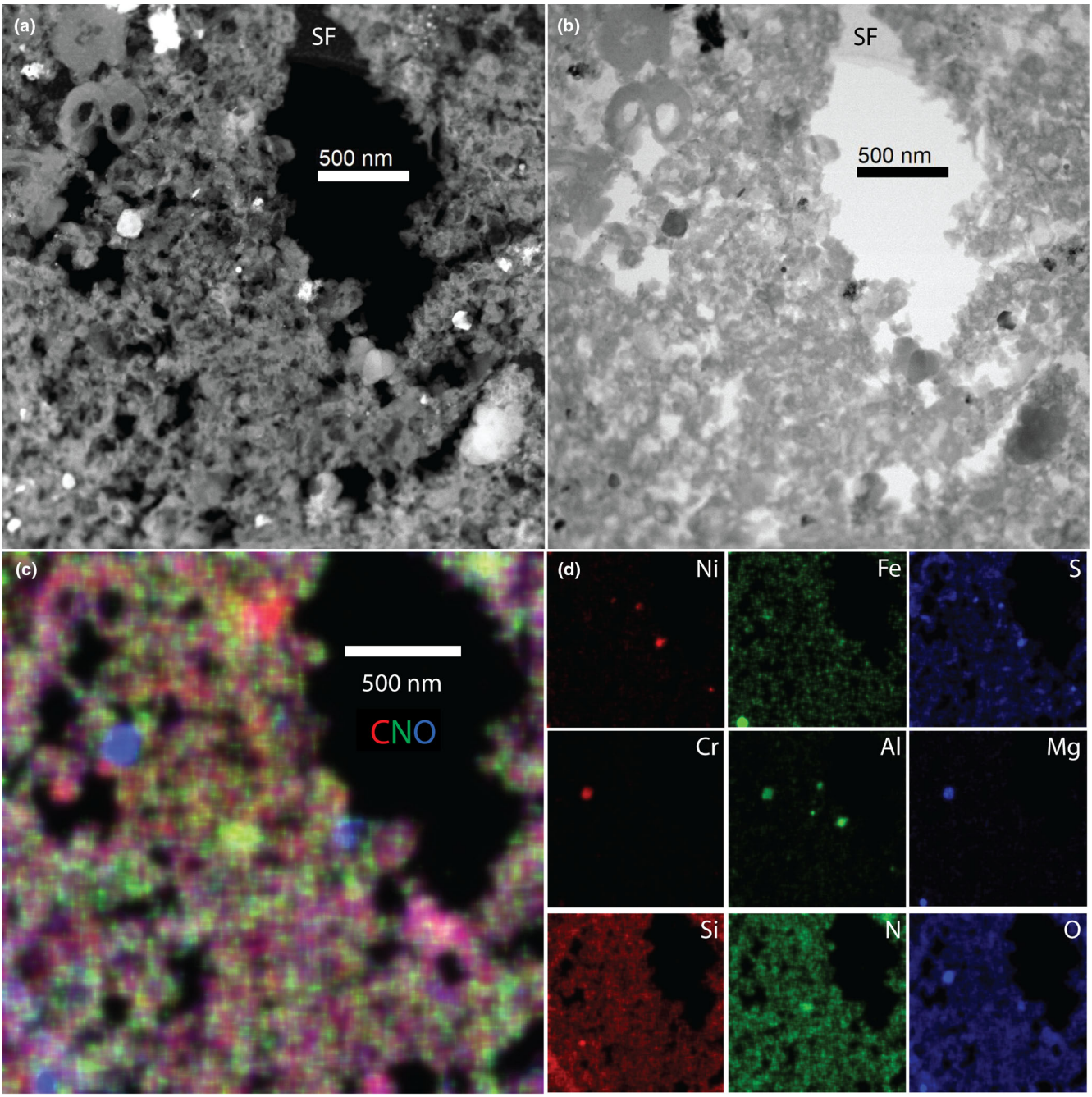

FIGURE 10. STEM imaging and EDS mapping of IOM residues. (a) HAADF image and (b) BF STEM image of microtomed IOM from C0107. The IOM shows abundant porous "fluffy" material, as well as hollow and solid nanoglobules. Nanoscale minerals, including spinels with variable Al, Mg, Cr and Fe and Fe,Ni sulfides, and SiC are present, and appear white in the HAADF image, black in the BF STEM images. (c) Composite EDS map (C [red], N [green] O [blue]) with 5× pixel smoothing revealing composition heterogeneity in the IOM at the 10 nm scale. (d) Individual EDS elemental maps for Ni, Fe, S, Cr, Al, Mg, Si, N, and O with 5× pixel smoothing reveal the locations of the nanoscale minerals retained in the IOM.

nanoglobules with diffuse boundaries that extend into the phyllosilicates may represent a combination of formation of the core globule at low temperature in the outer solar system (beyond the water ice snow line) and subsequent additional deposition of OM by C-rich parent body fluids contemporaneously with the alteration of the primary silicates.

Nanoglobules with multiple rims and heterogenous elemental composition indicate post-accretionary formation by C-rich fluids with a composition that

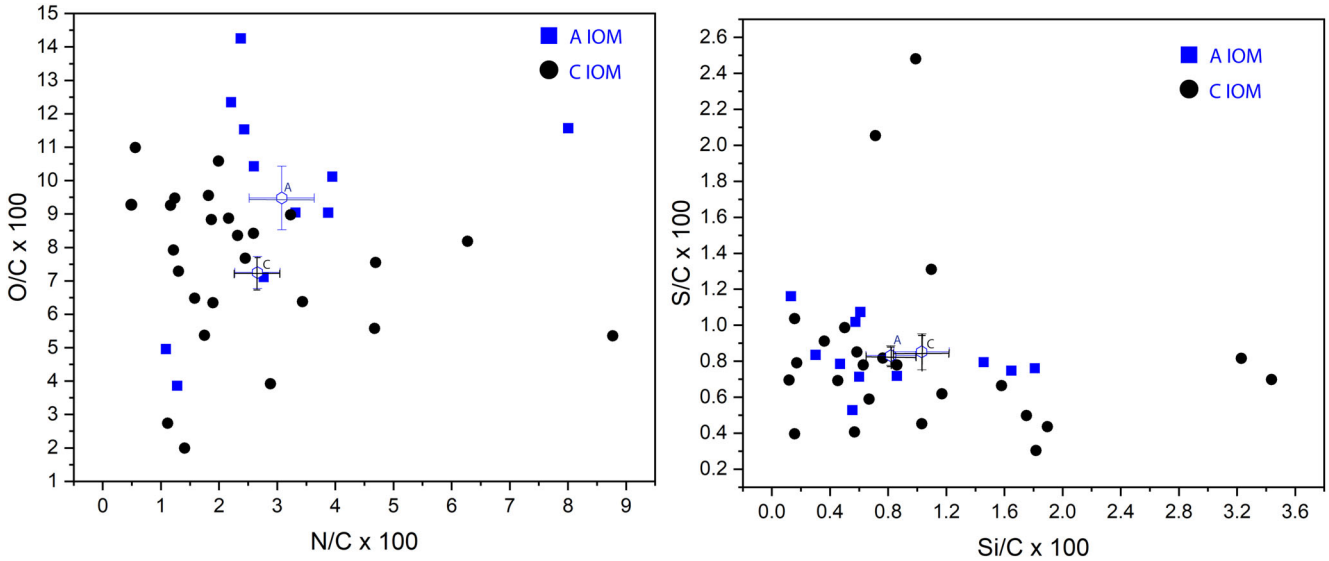

FIGURE 11. Compositional range of the microtomed IOM C0107 and A0106 samples in molar ratios determined from EDS analysis. All resolvable retained sulfide and oxide minerals were excluded from these analyses. The error bars indicate the mean value and SE of the mean for each ratio.

evolved over time, or through multiple fluid interaction events. Variation in N content as a function of nanoglobule diameter, as shown in Figure 3b, has been observed previously (Vollmer et al., 2014), but as-yet there are few measurements made with the necessary instrumentation and protocol to observe this variation.

The main challenges with quantitative N/C measurements are that N is difficult to detect by EDS and EELS at the 1% level in carbonaceous materials due to absorption of the N X-ray photons by the sample and by the window of the EDS detectors, and the large background from extended C K edge under the N edge in the EELS spectra. In addition, N is easily lost from the organics during EDS mapping under typical TEM conditions, that is, 0.2 nA probe current at 200 kV operating voltage. Future TEM measurements with windowless EDS detectors, at low operating voltages, 100 kV or less, or at standard voltages but using a cold stage to limit the N loss rate, could help constrain the range of nanoglobule origins and processing histories.

A definitive assignment of the processing history of all nanoglobules from among these scenarios is not possible with the current data set, and will require future coordinated isotopic, molecular, and structural studies. Nevertheless, the current data set on Ryugu samples provides a good basis for detailed comparison with IOM in meteorites and interplanetary dust particles carried out with similar methods. Overall, the characteristics of the nanoglobules from Ryugu are most similar to those from CI and CM meteorites, in terms of the globule shapes and chemistry, with less prominent ketone and carboxyl features than CO and CR meteorites (De Gregorio et al., 2013).

Phyllosilicate-Associated, or Clay-Bound Diffuse Carbon, with Molecular Carbonate Signature

Diffuse carbon, as used herein, is an umbrella term covering all of the OM without well-resolved particle boundaries, including coatings on phyllosilicate surfaces and intercalated between silicate sheets, coatings on other mineral grains, and nanoglobules or other particles too small to be resolved with TEM or XANES in typical FIB sections. Thus, diffuse carbon also represents multiple processes, as reflected in the variability of the functional group relative abundances. The aromatic, ketone, and carboxyl "IOM-like" portions of the diffuse OM are likely derived from the same sources and reaction pathways as the nanoglobules and dense irregular OM. The CO_3 carbonate feature at 290.4 eV is the one chemistry not represented in nanoglobules, requiring a different source or pathway. In our data, the CO_3 feature is readily observed in XANES spectra from FIB sections in regions of phyllosilicates, but completely absent from both XANES and EELS measurements of the demineralized IOM residues. The acid treatments used to isolate the IOM remove Si-rich minerals except for the rare SiC, as well as any carbonate minerals, so this loss does not provide additional constraint on the molecular or mineral carrier of the carbonate feature. In the sulfur-embedded particle ultramicrotome sections, the CO_3 feature is also seen with STEM-EELS localized to clay flakes, that is, mixtures of phyllosilicate and carbon.

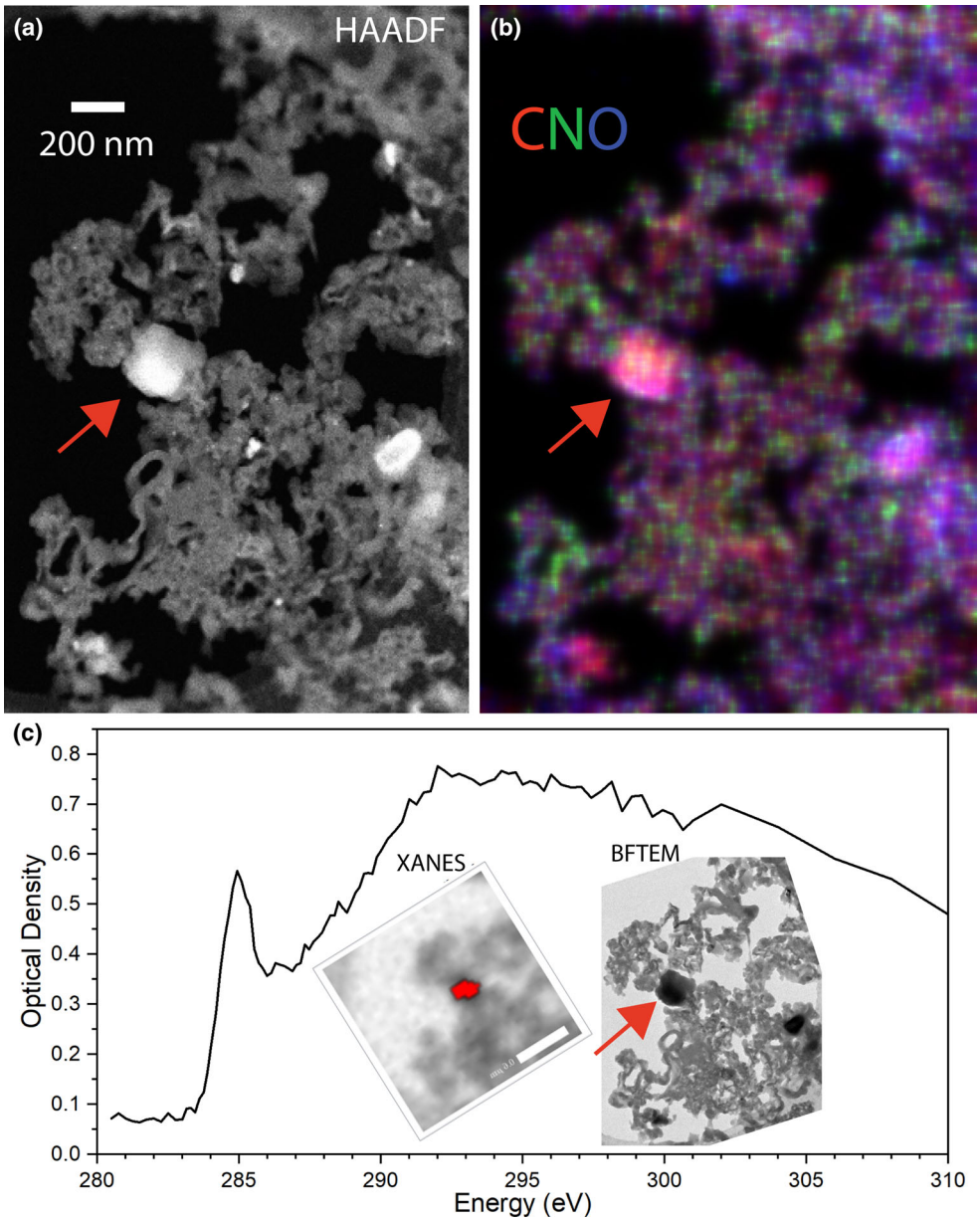

FIGURE 12. (a) HAADF STEM image of A0106 IOM. The red arrow indicates an ~150 nm sulfide particle with a coating of organic carbon. (b) STEM-EDS composite net count map C (red), N (green), O (blue). (c) C XANES sum spectrum from the particle. The summation region is indicated in red on the inset 296.7 eV XANES image. The IOM coating is aromatic.

These ultramicrotome sections are briefly exposed to neutral pH water, so the preservation of the CO_3 feature indicates that the CO_3 carrier is not strongly water soluble. Imaging of the individual thin clay flakes in TEM allows us to rule out the presence of carbonate mineral nanoparticles and confirm that CO_3 carrier is molecular. We also detected the CO_3 feature in a few individual clay flakes with XANES, but these data were signal limited by the low X-ray absorption signal of the <10 nm of C in the flakes.

One possible formation pathway for the molecular carbonate is by infiltration of CO_2-rich fluids into the phyllosilicates, and reaction with interlayer water to form H_2CO_3 and/or bonding with phyllosilicate cations to form $MgCO_3$ or $FeCO_3$. Clay-associated molecular carbonate was observed previously by Garvie and Buseck (2007), who used cold-stage transmission electron microscopy to study powdered and ultramicrotomed samples of CI (Ivuna and Orgueil) and Tagish Lake (C2-ungrouped) meteorites. These authors suggested that clay

minerals on asteroids may be important for catalyzing prebiotic molecule formation. Recent experimental work (Viennet et al., 2022) indicates reactions between the phyllosilicates and organic molecules are possible for Fe- and Al-rich clays at temperatures as low as 1000°C. The high Mg/Fe ratio in the Ryugu phyllosilicates and prevalence of Mg-carbonates suggests that Mg rather than Fe plays the greater role in the formation of the Ryugu molecular carbonates. However, this could depend on the local pH of the CO_2-rich fluids, as does the formation of carbonate minerals. The details of the atomic-scale nature of the carbonate and the asteroidal processes responsible for its formation remain important questions for future research.

Pockets of Preserved Primordial Organic Matter

Despite the extensive aqueous alteration, some of the OM retains primordial and even presolar signatures (Barosch et al., 2022). The nanodiamonds are indistinguishable in size and C K-edge features from nanodiamonds known to carry isotopic signatures (e.g., Xe-HL) of supernova origin, and thus, at least some of them may have presolar origins. Noble gas measurements of Ryugu samples have indicated a high abundance of Xe-HL from which a presolar diamond abundance of >4000 ppm has been estimated (Broadley et al., 2023). We found nanodiamonds in particles from both chamber A and chamber C, but the diamonds were clustered together in pockets of amorphous organic carbon, rather than distributed homogeneously, so the abundance may vary among regolith particles. The survival of the nanodiamond on Ryugu is not surprising, as it is resistant to aqueous alteration; the absence of nanodiamond would have indicated a significant departure from otherwise CI-like mineralogy. Larger presolar grains (SiC, graphite, oxides, and silicates) have also been identified in the Ryugu samples (Barosch et al., 2022; Ito et al., 2022; Nguyen et al., 2023).

Some isotopically anomalous OM particles are also preserved. The fractured nanoglobule/vermicular OM from A0108-11 in Figure 9 has anomalies in both D ($\delta D = 6700 \pm 500‰$) and N ($\delta^{15}N$ $358 \pm 30‰$) consistent with an outer solar system or molecular cloud origin (Yabuta et al., 2023, fig. S7d,e). The STEM-EELS data from this particle show it to be predominantly aromatic. In this case, the aromatic functional chemistry is likely primordial. In contrast, other particles (Figure 12) with aromatic chemistry are clearly revealed through TEM observations of the mineralogy to be products of aqueous alteration. While trends in the overall aromaticity and abundance can be correlated with the extent of hydrothermal parent body alteration, aromatic functional group chemistry of any individual particle does not uniquely constrain its origin in the absence of isotopic composition information.

Need for Complementary TEM Preparation and Analysis Protocols for Comprehensive Organic Matter Observations

As cautionary words for future studies, we note that reliable electron microscopy studies of the returned asteroid and meteorite samples are possible, but there is no single preparation (FIB, microtomed particle, or IOM isolate) or analysis method (60, 200, or 300 kV TEM or STEM, EDS, or EELS) that can be optimized for observation of all features of the OM. FIB sections, if prepared in way to limit electron beam heating and radiolysis (Bassim et al., 2012), can preserve functional chemistry including soluble components encapsulated in carrier minerals, but use of the electron beam to deposit the protective mask or to monitor the final thinning process can induce physical and chemical changes. Our results show that the molecular carbonate is present in FIB sections prepared using minimal alteration methods and in microtomed section and thus is not an artifact of the FIB process. However, this functional chemistry is lost in the IOM preparation process, likely due to the HF solubility of the phyllosilicate carrier and acid solubility of carbonate molecules. Depending on the degree of aqueous alteration, this molecular carbonate could represent a significant fraction of the total non-mineralic carbon, and at least partially explain the "missing carbon" question regarding the discrepancy between bulk meteorite carbon abundance, and the net carbon in IOM and SOM extracts (Alexander et al., 2017). Although the FIB can produce sections with preserved soluble components, the thickness of FIB sections has so far prevented their use for the observation of nanodiamonds, and other carbonaceous features at the few nm scale, including small nanoglobules. Given the biases introduced to the analyses by of each of the sample preparation methods, we recommend use of all three for the most comprehensive analysis. The use of TEM beam energies below the C=C displacement energy (~90 keV) under low-dose conditions or at higher energy with a cold stage and the new generation, high-sensitivity EDS, and EELS detectors is the best way to address the morphology, elemental composition and chemical bonding down to scales of individual diamonds.

CONCLUSIONS

Comprehensive transmission electron microscopy studies of sections of particles from both touchdown sites on asteroid Ryugu and extracted insoluble organic residues from particles A0106 and C0107 show that

Ryugu organic matter is consistent with the results from OM studies of primitive chondrites and is mostly similar to that of CI carbonaceous chondrites. No systematic differences between samples from Chambers A and C were observed, except for a marginally significantly higher O/C value for the A0106 IOM. All of the expected meteoritic OM morphologies are present, including nanoglobules, diffuse carbon, nonglobular particulate (vermicular and dense irregular), and nanodiamond, with abundant "fluffy" material in additional to nanoglobules in the demineralized IOM residues. One of the less expected results is that C-rich molecules that represent trapped parent body fluids and/or their products are preserved in vesicles in some secondary minerals at scales accessible to TEM analysis. Further analysis of such vesicles in the future may provide greater insight into early stages of hydrothermal alteration on asteroids. Additional analyses are also needed to better understand the molecular carbonate feature observed in EELS and XANES of diffuse carbon in FIB sections and clay flakes in ultramicrotomed sections, to determine the source of carbon, and the roles of specific cations (Mg and Fe) in the phyllosilicates. The morphological and chemical analysis of the OM shows that low-temperature hydrothermal alteration was pervasive, strongly shaping the diffuse carbon, and some nanoglobules. However, aliphatic carbon remains present, as do aromatic particles with isotopic signatures of outer solar system or molecular cloud origin.

Acknowledgments—We thank reviewer Christian Vollmer for helpful comments and suggestions for improving the manuscript. RMS acknowledges funding from NASA LARS Award 80NSSC23K0424. This research used beamline 5.3.2.2 of the Advanced Light Source, which is a DOE Office of Science User Facility under contract no. DE-AC02-05CH11231. JSPS KAKENHI grant numbers to TN related to this study are JP19H00725, JP19KK0094, and JP21H05424.

Data Availability Statement—The data that support the findings of this study are available from the corresponding author upon reasonable request.

Editorial Handling—Dr. Adrian John Brearley

REFERENCES

Alexander, C. M. O'D., Cody, G. D., Gregorio, B. T. D., Nittler, L. R., and Stroud, R. M. 2017. The Nature, Origin and Modification of Insoluble Organic Matter in Chondrites, the Major Source of Earth's C and N. *Chemie der Erde—Geochemistry* 77: 227–256.

Amari, S., Anders, E., Virag, A., and Zinner, E. 1990. Interstellar Graphite in Meteorites. *Nature* 345: 238–240.

Arakawa, M., Saiki, T., Wada, K., Ogawa, K., Kadono, T., Shirai, K., Sawada, H., et al. 2020. An Artificial Impact on the Asteroid (162173) Ryugu Formed a Crater in the Gravity-Dominated Regime. *Science* 368: 67–71.

Barosch, J., Nittler, L. R., Wang, J., Alexander, C. M. O'D., De Gregorio, B. T., Engrand, C., Kebukawa, Y., et al. 2022. Presolar Stardust in Asteroid Ryugu. *The Astrophysical Journal Letters* 935: L3.

Bassim, N. D., De Gregorio, B. T., Kilcoyne, A. L. D., Scott, K., Chou, T., Wirick, S., Cody, G., and Stroud, R. M. 2012. Minimizing Damage during FIB Sample Preparation of Soft Materials. *Journal of Microscopy* 245: 288–301.

Brearley, A. J. 1999. Origin of Graphitic Carbon and Pentlandite in Matrix Olivines in the Allende Meteorite. *Science* 285: 1380–82.

Brearley, A. J. 2021. Nanophase Iron Carbides in Fine-Grained Rims in CM2 Carbonaceous Chondrites: Formation of Organic Material by Fischer–Tropsch Catalysis in the Solar Nebula. *Meteoritics & Planetary Science* 56: 108–126.

Broadley, M. W., Byrne, D. J., Füri, E., Zimmermann, L., Marty, B., Okazaki, R., Yada, T., et al. 2023. The Noble Gas and Nitrogen Relationship between Ryugu and Carbonaceous Chondrites. *Geochimica et Cosmochimica Acta* 345: 62–74.

Cody, G. D., Ade, H., Alexander, C. M. O'D., Araki, T., Butterworth, A., Fleckenstein, H., Flynn, G. J., et al. 2008. Quantitative Organic and Light-Element Analysis of Comet 81P/Wild 2 Particles Using C-, N-, and O-Mu - XANES. *Meteoritics & Planetary Science* 43: 353–365.

Cody, G. D., and Alexander, C. M. O'D. 2005. NMR Studies of Chemical Structural Variation of Insoluble Organic Matter from Different Carbonaceous Chondrite Groups. *Geochimica et Cosmochimica Acta* 69: 1085–97.

Coffey, T., Urquhart, S. G., and Ade, H. 2002. Characterization of the Effects of Soft X-Ray Irradiation on Polymers. *Journal of Electron Spectroscopy and Related Phenomena* 122: 65–78.

Daly, L., Lee, M. R., Bland, P. A., Smith, W., McFadzean, S., Martin, P.-E., Bagot, P. A. J., et al. 2022. Interaction between Phyllosilicates and Organic Nanoglobules in Ryugu. 53rd Lunar and Planetary Science Conference, p. 2258 Abstract # 2678.

De Gregorio, B. T., Alexander, C. M. O'D., and Stroud, R. M. 2019. Analysis of In Situ Nanodiamonds in Organic Matter from Primitive Meteorites with Electron Energy-Loss Spectroscopy and Energy Dispersive X-Ray Spectroscopy. *Microscopy and Microanalysis* 25: 2456–57.

De Gregorio, B. T., Stroud, R. M., Nittler, L. R., Alexander, C. M. O'D., Bassim, N. D., Cody, G. D., Kilcoyne, A. L. D., et al. 2013. Isotopic and Chemical Variation of Organic Nanoglobules in Primitive Meteorites. *Meteoritics & Planetary Science* 48: 804–828.

Ferguson, F. T., Johnson, N. M., Abreu, N., and Nuth, J. A. 2021. The Formation of Carbonaceous Material in the Early Solar Nebula: The Role of Metal Dusting. *The Astrophysical Journal* 908: 48.

Floss, C., Le Guillou, C., and Brearley, A. 2014. Coordinated NanoSIMS and FIB-TEM Analyses of Organic Matter and Associated Matrix Materials in CR3 Chondrites. *Geochimica et Cosmochimica Acta* 139: 1–25.

Garvie, L. A. J. 2010. Where are the Nanodiamonds in the Primitive Meteorites? *41st Lunar and Planetary Science Conference*, Abstract # 1388.

Garvie, L. A. J., and Buseck, P. R. 2007. Prebiotic Carbon in Clays from Orgueil and Ivuna (CI), and Tagish Lake (C2 Ungrouped) Meteorites. *Meteoritics & Planetary Science* 42: 2111–17.

Hashiguchi, M., Kobayashi, S., and Yurimoto, H. 2013. In Situ Observation of D-Rich Carbonaceous Globules Embedded in NWA 801 CR2 Chondrite. *Geochimica et Cosmochimica Acta* 122: 306–323.

Ito, M., Tomioka, N., Uesugi, M., Yamaguchi, A., Shirai, N., Ohigashi, T., Liu, M.-C., et al. 2022. A Pristine Record of Outer Solar System Materials from Asteroid Ryugu's Returned Sample. *Nature Astronomy* 6: 1163–71.

Kebukawa, Y., Ito, M., Zolensky, M. E., Greenwood, R. C., Rahman, Z., Suga, H., Nakato, A., et al. 2019. A Novel Organic-Rich Meteoritic Clast from the Outer Solar System. *Science Report* 9: 3169.

Kitazato, K., Milliken, R. E., Iwata, T., Abe, M., Ohtake, M., Matsuura, S., Arai, T., et al. 2019. The Surface Composition of Asteroid 162173 Ryugu from Hayabusa2 near-Infrared Spectroscopy. *Science* 364: 272–75.

Kitazato, K., Milliken, R. E., Iwata, T., Abe, M., Ohtake, M., Matsuura, S., Takagi, Y., et al. 2021. Thermally Altered Subsurface Material of Asteroid (162173) Ryugu. *Nature Astronomy* 5: 246–250.

Le Guillou, C., Bernard, S., Brearley, A. J., and Remusat, L. 2014. Evolution of Organic Matter in Orgueil, Murchison and Renazzo during Parent Body Aqueous Alteration: In Situ Investigations. *Geochimica et Cosmochimica Acta* 131: 368–392.

Lewis, R. S., Ming, T., Wacker, J. F., Anders, E., and Steel, E. 1987. Interstellar Diamonds in Meteorites. *Nature* 326: 160–62.

Matsuoka, M., Kagawa, E.-I., Amano, K., Nakamura, T., Tatsumi, E., Osawa, T., Hiroi, T., et al. 2023. Space Weathering Acts Strongly on the Uppermost Surface of Ryugu. *Communications Earth & Environment* 4: 335.

Nakamura, E., Kobayashi, K., Tanaka, R., Kunihiro, T., Kitagawa, H., Potiszil, C., Ota, T., et al. 2022. On the Origin and Evolution of the Asteroid Ryugu: A Comprehensive Geochemical Perspective. *Proceedings of the Japan Academy, Series B* 98: 227–282.

Nakamura, T., Matsumoto, M., Amano, K., Enokido, Y., Zolensky, M. E., Mikouchi, T., Genda, H., et al. 2023. Formation and Evolution of Carbonaceous Asteroid Ryugu: Direct Evidence from Returned Samples. *Science* 379: eabn8671.

Nakamura-Messenger, K., Messenger, S., Keller, L. P., Clemett, S. J., and Zolensky, M. E. 2006. Organic Globules in the Tagish Lake Meteorite: Remnants of the Protosolar Disk. *Science* 314: 1439–42.

Naraoka, H., Takano, Y., Dworkin, J. P., Oba, Y., Hamase, K., Furusho, A., Ogawa, N. O., et al. 2023. Soluble Organic Molecules in Samples of the Carbonaceous Asteroid (162173) Ryugu. *Science* 379: eabn9033.

Nguyen, A. N., Mane, P., Keller, L. P., Piani, L., Abe, Y., Aléon, J., Alexander, C. M. O'D., et al. 2023. Abundant Presolar Grains and Primordial Organics Preserved in Carbon-Rich Exogenous Clasts in Asteroid Ryugu. *Science Advances* 9: eadh1003.

Noguchi, T., Matsumoto, T., Miyake, A., Igami, Y., Haruta, M., Saito, H., Hata, S., et al. 2023. A Dehydrated Space-Weathered Skin Cloaking the Hydrated Interior of Ryugu. *Nature Astronomy* 7: 170–181.

Okazaki, R., Marty, B., Busemann, H., Hashizume, K., Gilmour, J. D., Meshik, A., Yada, T., et al. 2023. Noble Gases and Nitrogen in Samples of Asteroid Ryugu Record its Volatile Sources and Recent Surface Evolution. *Science* 379: eabo0431.

Pieters, C. M., and Noble, S. K. 2016. Space Weathering on Airless Bodies. *Journal of Geophysical Research: Planets* 121: 1865–84.

Srot, V., Wegst, U. G. K., Salzberger, U., Koch, C. T., Hahn, K., Kopold, P., and van Aken, P. A. 2013. Microstructure, Chemistry, and Electronic Structure of Natural Hybrid Composites in Abalone Shell. *Micron* 48: 54–64.

Stroud, R., De Gregorio, B., and Alexander, C. M. O'D. 2021. Coordinated Electron Energy Loss and Energy Dispersive X-Ray Spectroscopies of Organic Matter from Asteroids. *Microscopy and Microanalysis* 27: 2546–47.

Sugita, S., Honda, R., Morota, T., Kameda, S., Sawada, H., Tatsumi, E., Yamada, M., et al. 2019. The Geomorphology, Color, and Thermal Properties of Ryugu: Implications for Parent-Body Processes. *Science* 364: eaaw0422.

Tachibana, S., Sawada, H., Okazaki, R., Takano, Y., Sakamoto, K., Miura, Y. N., Okamoto, C., et al. 2022. Pebbles and Sand on Asteroid (162173) Ryugu: In Situ Observation and Particles Returned to Earth. *Science* 375: 1011–16 early view.

Viennet, J. C., Le Guillou, C., Remusat, L., Baron, F., Delbes, L., Blanchenet, A. M., Laurent, B., Criouet, I., and Bernard, S. 2022. Experimental Investigation of Fe-Clay/Organic Interactions under Asteroidal Conditions. *Geochimica et Cosmochimica Acta* 318: 352–365.

Vollmer, C., Kepaptsoglou, D., Leitner, J., Busemann, H., Spring, N. H., Ramasse, Q. M., Hoppe, P., and Nittler, L. R. 2014. Fluid-Induced Organic Synthesis in the Solar Nebula Recorded in Extraterrestrial Dust from Meteorites. *Proceedings of the National Academy of Sciences of the United States of America* 111: 343.

Yabuta, H., Cody, G. D., Engrand, C., Kebukawa, Y., De Gregorio, B., Bonal, L., Remusat, L., et al. 2023. Macromolecular Organic Matter in Samples of the Asteroid (162173) Ryugu. *Science* 379: eabn9057.

Yokoyama, T., Nagashima, K., Nakai, I., Young, E. D., Abe, Y., Aléon, J., Alexander, C. M. O'D., et al. 2023. Samples Returned from the Asteroid Ryugu are Similar to Ivuna-Type Carbonaceous Meteorites. *Science* 379: eabn7850.